

Cloud Drop Number Concentrations over the Western North Atlantic Ocean: Seasonal Cycle, Aerosol Interrelationships, and Other Influential Factors

Hossein Dadashazar¹, David Painemal^{2,3}, Majid Alipanah⁴, Michael Brunke⁵, Seethala Chellappan⁶, Andrea F. Corral¹, Ewan Crosbie^{2,3}, Simon Kirschler⁷, Hongyu Liu⁸, Richard Moore², Claire Robinson^{2,3}, Amy Jo Scarino^{2,3}, Michael Shook², Kenneth Sinclair^{9,10}, K. Lee Thornhill², Christiane Voigt⁷, Hailong Wang¹¹, Edward Winstead^{2,3}, Xubin Zeng⁵, Luke Ziemba², Paquita Zuidema⁶, Armin Sorooshian^{1,5}

¹Department of Chemical and Environmental Engineering, University of Arizona, Tucson, AZ, USA

²NASA Langley Research Center, Hampton, VA, USA

³Science Systems and Applications, Inc., Hampton, VA, USA

⁴Department of Systems and Industrial Engineering, University of Arizona, Tucson, AZ, USA

⁵Department of Hydrology and Atmospheric Sciences, University of Arizona, Tucson, AZ, USA

⁶Rosenstiel School of Marine and Atmospheric Science, University of Miami, Miami, FL, USA

⁷Institute of Atmospheric Physics, German Aerospace Center

⁸National Institute of Aerospace, Hampton, VA, USA

⁹NASA Goddard Institute for Space Studies, New York, NY, USA

¹⁰Universities Space Research Association, Columbia, MD, USA

¹¹Atmospheric Sciences and Global Change Division, Pacific Northwest National Laboratory, Richland, WA, USA

*Correspondence to: Hossein Dadashazar (hosseind@arizona.edu)

Abstract. Cloud drop number concentrations (N_d) over the western North Atlantic Ocean (WNAO) are generally highest during the winter (DJF) and lowest in summer (JJA), in contrast to aerosol proxy variables (aerosol optical depth, aerosol index, surface aerosol mass concentrations, surface cloud condensation nuclei [CCN] concentrations) that generally peak in spring (MAM) and JJA with minima in DJF. Using aircraft, satellite remote sensing, ground-based in situ measurements data as well as reanalysis data, we characterize factors explaining the divergent seasonal cycles and furthermore probe into factors influencing N_d on seasonal time scales. The results can be summarized well by features most pronounced in DJF, including features associated with cold air outbreak (CAO) conditions such as enhanced values of CAO index, planetary boundary layer height (PBLH), low-level liquid cloud fraction, and cloud-top height, in addition to winds aligned with continental outflow. Data sorted into high and low N_d days in each season, especially in DJF, revealed that all of these conditions were enhanced on the high N_d days, including reduced sea level pressure and stronger wind speeds. Although aerosols may be more abundant in MAM and JJA, the conditions needed to activate those particles into cloud droplets are weaker than in colder months, which is demonstrated by calculations of strongest (weakest) aerosol indirect effects in DJF (JJA) based on comparing N_d to perturbations in four different aerosol proxy variables (total and sulfate aerosol optical depth, aerosol index, surface mass concentration of sulfate). We used three machine learning models and up to 12 input variables to infer about most influential factors related to N_d for DJF and JJA, with the best performance obtained with gradient boosted regression tree (GBRT) analysis. The model results indicated that cloud fraction was the most important input variable, followed by some combination (depending on season) of CAO index and surface mass concentrations of sulfate and organic carbon. Future work is recommended to further understand aspects uncovered here such as impacts of free tropospheric aerosol entrainment on clouds, [degree of boundary layer coupling](#), wet scavenging and giant CCN effects on aerosol- N_d relationships, updraft velocity, and vertical structure of cloud properties such as adiabaticity that impact the satellite estimation of N_d .

1. Introduction

Aerosol indirect effects remain the dominant source of uncertainty in estimates of total anthropogenic radiative forcing (Myhre et al., 2013; Boucher et al., 2013; Myhre et al., 2013). Central to these effects is knowledge about cloud drop number concentration (N_d), as it is the connection between the subset of particles that activate into drops (cloud condensation nuclei, CCN) and cloud properties. It is widely accepted that warm clouds influenced by higher number concentrations of aerosol particles have potentially elevated N_d and smaller drops (all else held fixed), ~~potentially~~ resulting in enhanced cloud albedo at fixed liquid water path (Twomey, 1977), and potentially suppressed precipitation (Albrecht, 1989), and increased vulnerability to overlying air resulting from enhanced cloud top entrainment (Ackerman et al., 2004).

Reducing uncertainty in how aerosols and clouds interact within a given meteorological context requires accurate estimates of N_d and aerosol concentrations and properties. Since intensive field studies struggle to obtain broad spatial and temporal coverage of such data, satellite remote sensing and reanalysis datasets are relied on for studies examining intra- and interannual features over large spatial areas. Limitations of satellite retrievals are important to recognize. N_d is not directly retrieved but derived using other parameters (e.g., cloud optical depth, cloud drop effective radius, cloud top temperature) and with assumptions about cloud adiabatic growth and N_d being vertically constant (Grosvenor et al., 2018). Aerosol number concentrations are usually represented by a columnar parameter such as aerosol optical depth (AOD) and thus not directly below clouds, which is the aerosol layer most likely to interact with the clouds. Furthermore, aerosol data are difficult to retrieve in cloudy columns. Reanalysis datasets circumvent issues for the aerosol parameters as they provide vertically-resolved data (e.g., surface layer and thus below clouds) and are available for cloudy columns.

Of special interest in this work is the western North Atlantic Ocean (WNAO) where decades of extensive research have been conducted for topics largely unrelated to aerosol-cloud interactions (Sorooshian et al., 2020), thereby providing opportunity for closing knowledge gaps for this area in a region with a wide range of aerosol and meteorological conditions (Corral et al., 2021; Painemal et al., 2021). Past work showed different seasonal cycles of AOD and N_d in this region (Grosvenor et al., 2018; Sorooshian et al., 2019; ~~Grosvenor et al., 2018~~), which partly motivates this study to unravel why N_d behaves differently on seasonal time scales. A previous study investigating seasonal cycles of N_d in the North Atlantic region found that cloud microphysical properties were primarily dependent on CCN concentrations while cloud macrophysical properties were more dependent on meteorological conditions (e.g., Sinclair et al., 2020). However, due to the complexity of interactions involved and the co-variability between individual components, the magnitude and sign of these feedbacks remain uncertain.

This study uses a multitude of datasets to characterize the N_d seasonal cycle and factors related to N_d variability. The structure of the results and discussion are as follows: (i) case study flight highlighting the wide range of N_d in wintertime and factors potentially affecting that variability; (ii) seasonal cycle of N_d and aerosol concentrations based on different proxy variables; (iii) seasonal cycles of factors potentially influential for N_d such as aerosol size distribution, vertical distribution of aerosol, humidity effects, and aerosol-cloud interactions; (iv) composite analysis of influential factors on “high” and “low” N_d days in each season; (v) modeling analysis to probe more deeply into N_d relationships with other parameters for winter and summer seasons; and (vi) discussion of other factors relevant to N_d unexplored in this work.

2. Methods

2.1 Study Region

We focus on the WNAO, defined here as being bounded by 25° – 50°N and 60° – 85°W. A subset of the results focuses on 6 individual sub-domains representative of different parts of the WNAO (shown later), with five just off the East Coast extending from south to north (South = S, Central-South = C-S, Central = C, Central-North = C-N, North = N) and one over Bermuda.

2.2 Datasets

2.2.1 Satellite Observations (CERES-MODIS/CALIPSO)

Relevant cloud parameters were obtained from the Clouds and the Earth's Radiant Energy System (CERES) edition 4 products (Minnis et al., 2011; Minnis et al., 2020), which are based on the application of CERES's retrieval algorithms on the radiances measured by the MODerate resolution Imaging Spectroradiometer (MODIS) instrument aboard the Aqua satellite. ~~The Aqua observations used here to estimate N_d were from the daytime overpasses of the satellite around 13:30 of (local time) for nadir observations.~~ Level 3 daily cloud properties at 1° × 1° spatial resolution (listed in Table 1) were used for the period between January 2013 and December 2017 from CERES-MODIS edition 4 Single Scanning Footprint (SSF) products (Loeb et al., 2016). ~~The CERES-MODIS SSF Level 3 product includes 1° × 1° averaged data according to the cloud top pressure of individual pixels into: low (heights below 700 hPa), mid-low (heights within 700–500 hPa), mid-high (heights within 500–300 hPa), and high (heights above 300 hPa) level clouds. For this study, we only use low-cloud averages.~~

N_d is estimated based on an adiabatic cloud model (Grosvenor et al., 2018):

$$N_d = \frac{\sqrt{5}}{2 \pi k} \left(\frac{f_{ad} C_w \tau}{Q_{ext} \rho_w r_e} \right)^{1/2} \quad (1)$$

where τ is cloud optical depth and r_e is cloud drop effective radius, both of which are obtained from CERES-MODIS for low-level (i.e., surface to 700 hPa) liquid clouds. Q_{ext} is the unitless extinction efficiency factor, assumed to be 2 for liquid cloud droplets, and ρ_w is the density of water (1 g cm⁻³). Methods described in Painemal (2018) were used to estimate parameters in Eq. 1 as follows: (i) adiabatic water lapse rate (C_w) was determined using cloud top pressure and temperature provided by CERES-MODIS; (ii) the N_d estimation is often corrected for the sub-adiabatic profile by applying the adiabatic value (f_{ad}), but in this work, a value of $f_{ad} = 1$ was assumed due to both lack of consensus on its value and its relatively minor impact on N_d estimation (Grosvenor et al., 2018); and (iii) k parameter representing the width of the droplet spectrum was assumed to be 0.8 over the ocean. Statistics of N_d are often estimated after screening daily observations based on cloud fractions (Wood, 2012; Grosvenor et al., 2018). The purpose of such filters is to reduce the uncertainties associated with the estimation of N_d (Eq. 1) driven by the errors in the retrieval of r_e and τ from MODIS's observed reflectance in a highly heterogeneous cloud field. However, this may unwantedly mask the effects of cloud regime on aerosol-cloud interactions by only including certain low-level cloud types in the analyses (e.g., closed-cell stratocumulus). Therefore, we use all N_d data regardless of cloud fraction with exceptions being Sections 3.5 and 4.2 where a filter of low-level liquid cloud fraction (i.e., $CF_{low-liq} \geq 0.1$) was applied.

The Cloud-Aerosol Lidar with Orthogonal Polarization (CALIOP) instrument aboard the Cloud-Aerosol Lidar and Infrared Pathfinder Satellite Observations (CALIPSO) provides data on

Formatted: Subscript

Formatted: Font: (Default) +Headings CS (Times New Roman), Font color: Text 1, Complex Script Font: +Headings CS (Times New Roman), Bold

Formatted: Font: (Default) +Headings CS (Times New Roman), Font color: Text 1, Complex Script Font: +Headings CS (Times New Roman), Bold

Formatted: Font: (Default) +Headings CS (Times New Roman), Font color: Text 1, Complex Script Font: +Headings CS (Times New Roman), Bold

Formatted: Font: (Default) +Headings CS (Times New Roman), Font color: Text 1, Complex Script Font: +Headings CS (Times New Roman), Bold

147 the vertical distribution of aerosols (Winker et al., 2009). Nighttime extinction profiles were
148 acquired from Level 2 version 4.20 products (i.e., 5 km aerosol profile data), between January
149 2013 and December 2017. We averaged the Level 2 daily extinctions in different $4^\circ \times 5^\circ$ sub-
150 domains (shown later) to obtain the seasonal profiles after applying the screening scheme outlined
151 in Tackett et al. (2018).

Table 1: Summary of various data products used in this study.

Parameter	Data Source	Spatial resolution	Vertical level	Date Range	Spatial Area	Temporal resolution
Cloud optical thickness	CERES-MODIS	1°x1°	NA	01-Jan-2013 31-Dec-2017	60°-85°W; 25°-50°N	Daily
Cloud effective radius	CERES-MODIS	1°x1°	NA	01-Jan-2013 31-Dec-2017	60°-85°W; 25°-50°N	Daily
Cloud fraction	CERES-MODIS	1°x1°	NA	01-Jan-2013 31-Dec-2017	60°-85°W; 25°-50°N	Daily
Cloud top temperature	CERES-MODIS	1°x1°	NA	01-Jan-2013 31-Dec-2017	60°-85°W; 25°-50°N	Daily
Cloud effective height	CERES-MODIS	1°x1°	NA	01-Jan-2013 31-Dec-2017	60°-85°W; 25°-50°N	Daily
Cloud top pressure	CERES-MODIS	1°x1°	NA	01-Jan-2013 31-Dec-2017	60°-85°W; 25°-50°N	Daily
Precipitation	PERSIANN-CDR	1°x1°	NA	01-Jan-2013 31-Dec-2017	60°-85°W; 25°-50°N	Daily
Aerosol extinction (532 nm)	CALIPSO/CALIP	1°x1°	NA	01-Jan-2013 31-Dec-2017	60°-85°W; 25°-50°N	Daily
Total aerosol extinction AOT (550 nm)	MERRA-2	5 km	NA	01-Jan-2013 31-Dec-2017	60°-85°W; 25°-50°N	Daily
Total aerosol Angstrom parameter (470-870 nm)	MERRA-2	1°x1°	NA	01-Jan-2013 31-Dec-2017	60°-85°W; 25°-50°N	Daily
Sulfate extinction AOT (550 nm)	MERRA-2	1°x1°	NA	01-Jan-2013 31-Dec-2017	60°-85°W; 25°-50°N	Daily
Sea-salt extinction AOT (550 nm)	MERRA-2	1°x1°	NA	01-Jan-2013 31-Dec-2017	60°-85°W; 25°-50°N	Daily
Dust extinction AOT (550 nm)	MERRA-2	1°x1°	NA	01-Jan-2013 31-Dec-2017	60°-85°W; 25°-50°N	Daily
Organic carbon extinction AOT (550 nm)	MERRA-2	1°x1°	NA	01-Jan-2013 31-Dec-2017	60°-85°W; 25°-50°N	Daily
Black carbon extinction AOT (550 nm)	MERRA-2	1°x1°	NA	01-Jan-2013 31-Dec-2017	60°-85°W; 25°-50°N	Daily
Sulfate surface mass concentration	MERRA-2	1°x1°	NA	01-Jan-2013 31-Dec-2017	60°-85°W; 25°-50°N	Daily
Sea-salt surface mass concentration	MERRA-2	1°x1°	NA	01-Jan-2013 31-Dec-2017	60°-85°W; 25°-50°N	Daily
Dust surface mass concentration	MERRA-2	1°x1°	NA	01-Jan-2013 31-Dec-2017	60°-85°W; 25°-50°N	Daily
Organic carbon surface mass concentration	MERRA-2	1°x1°	NA	01-Jan-2013 31-Dec-2017	60°-85°W; 25°-50°N	Daily
Black carbon surface mass concentration	MERRA-2	1°x1°	NA	01-Jan-2013 31-Dec-2017	60°-85°W; 25°-50°N	Daily
Sea level pressure	MERRA-2	1°x1°	Surface	01-Jan-2013 31-Dec-2017	60°-85°W; 25°-50°N	Daily
Geopotential height	MERRA-2	1°x1°	850 hPa	01-Jan-2013 31-Dec-2017	60°-85°W; 25°-50°N	Daily
Sea surface temperature	MERRA-2	1°x1°	Sea surface	01-Jan-2013 31-Dec-2017	60°-85°W; 25°-50°N	Daily
Air temperature	MERRA-2	1°x1°	Surface, 850, 700 hPa	01-Jan-2013 31-Dec-2017	60°-85°W; 25°-50°N	Daily
Relative humidity	MERRA-2	1°x1°	1000-500 hPa	01-Jan-2013 31-Dec-2017	60°-85°W; 25°-50°N	Daily
Wind speed	MERRA-2	1°x1°	2 meter, 950 hPa	01-Jan-2013 31-Dec-2017	60°-85°W; 25°-50°N	Daily
Planetary boundary layer height	MERRA-2	1°x1°	NA	01-Jan-2013 31-Dec-2017	60°-85°W; 25°-50°N	Daily
Vertical pressure velocity	MERRA-2	1°x1°	800 hPa	01-Jan-2013 31-Dec-2017	60°-85°W; 25°-50°N	Daily
Aerosol/Cloud	Arbome: ACTIVATE	-	NA	22-Feb-2020	72.31°-76.64°W; 34.08°-37.16°N	1 Second
CCN-Cape Cod	Ground based measurement	Point measurement	Surface	16-Jul-2012 04-May-2013	70.30°W; 41.67°N	1 Second

2.2.2 MERRA-2

Aerosol data were obtained from the Modern-Era Retrospective analysis for Research and Applications-Version 2 (MERRA-2) (Gelaro et al., 2017). MERRA-2 is a multidecadal reanalysis where meteorological and aerosol observations are jointly assimilated into the Goddard Earth Observation System version 5 (GEOS-5) data assimilation system (Randles et al., 2017; Buchard et al., 2017; Randles et al., 2017). Aerosols in MERRA-2 are simulated with a radiatively coupled version of the Goddard Chemistry, Aerosol, Radiation, and transport model (GOCART; Chin et al., 2002; Colarco et al., 2010). GOCART treats the sources, sinks, and chemistry of 15 externally mixed aerosol mass mixing ratio tracers, which include sulfate, hydrophobic and hydrophilic black and organic carbon, dust (five size bins), and sea salt (five size bins). MERRA-2 includes assimilation of bias-corrected Collection 5 MODIS AOD, bias-corrected AOD from the Advanced Very High Resolution Radiometer (AVHRR) instruments, AOD retrievals from the Multiangle Imaging SpectroRadiometer (MISR) over bright surfaces, and ground-based Aerosol Robotic Network (AERONET) direct measurements of AOD (Gelaro et al., 2017). In this study we used total and speciated (i.e., sea-salt, dust, black carbon, organic carbon, and sulfate) AOD at 550 nm between January 2013 and December 2017 at times relevant to Aqua's overpass time (13:30 local time). Aerosol index was calculated as the product of AOD and Ångström parameter. MERRA-2 also provides surface mass concentrations of aerosol species including sea-salt, dust, black carbon, organic carbon, and sulfate, which were used as a measure of aerosol levels in the planetary boundary layer (PBL).

MERRA-2 data were also used for environmental variables including both thermodynamic (e.g., temperature and relative humidity) and dynamic parameters (e.g., sea-level pressure (SLP) and geopotential heights) (Gelaro et al., 2017) listed in Table 1. Bilinear interpolation was applied to transfer all MERRA-2 variables (Table 1) from their original $0.5^\circ \times 0.625^\circ$ spatial resolution to the equivalent $1^\circ \times 1^\circ$ grid in CERES-MODIS Level 3 data.

2.2.3 Precipitation Data

Daily precipitation data were obtained from Precipitation Estimation from Remotely Sensed Information using Artificial Neural Networks–Climate Data Record (PERSIANN-CDR) data product (Ashouri et al., 2015; Nguyen et al., 2018). Bilinear interpolation was applied to convert the PERSIANN-CDR data from its native spatial resolution (i.e., $0.25^\circ \times 0.25^\circ$) to equivalent $1^\circ \times 1^\circ$ grids in CERES-MODIS Level 3 data. It is important to note that we use daily averaged PERSIANN-CDR provides daily estimate of precipitation and, therefore, there is some level-temporal mismatch/offset between precipitation data and with the daily N_d value from MODIS-Aqua that comes at one time of the day. This can contribute to some level of uncertainty for the discussions based on analyses that involved studying the involving relationships between precipitation and N_d .

2.2.4 Surface-based CCN Data

Cloud condensation nuclei (CCN) data were obtained from the U.S. Department of Energy's Two-Column Aerosol Project (TCAP) (Berg et al., 2016) to examine the seasonal variations in CCN number concentration at a representative site by Cape Cod, Massachusetts (41.67°N , 70.30°W) over the U.S. East Coast. TCAP was a campaign conducted between June 2012 and June 2013 to investigate aerosol optical and physicochemical properties and interactions between aerosols and clouds (Berg et al., 2016; Liu and Li, 2019; Berg et al., 2016). CCN data

Formatted: Subscript

were available between July 2012 and May 2013 at multiple supersaturations with some gaps in the data collection (i.e., November–December); for simplicity, we focused on CCN data measured at a single supersaturation of 1% owing to relatively better data coverage as compared to lower supersaturations. We note that this higher supersaturation is not necessarily representative of that relevant to the clouds of interest, but is still insightful for understanding the seasonal cycle of CCN concentration. The qualitative seasonal cycle of CCN concentration at 1% matches those at lower supersaturations (e.g., 0.15% – 0.8%).

2.2.5 Airborne In-Situ Data

We used airborne in-situ data collected during the fifth research flight (RF05) of the Aerosol Cloud Meteorology Interactions over the western Atlantic Experiment (ACTIVATE) campaign. One flight is used both for simplicity and because it embodied conditions relevant to the discussion of other results. The mission concept involves joint flights between the NASA Langley UC-12 King Air and HU-25 Falcon such that the former flies around 8 – 10 km and the latter flies in the boundary layer to simultaneously collect data on aerosol, cloud, gas, and meteorological parameters in the same column (Sorooshian et al., 2019). The Falcon flew in a systematic way to collect data at different vertical regions relative to cloud, including the following of relevance to this study: BCB = below cloud base; ACB = above cloud base, BCT = below cloud top, Min. Alt = minimum altitude the plane flies at (500 ft).

This study makes use of the HU-25 Falcon data from the following instruments: Fast Cloud Droplet Probe (FCDP; $D_p \sim 3 - 50 \mu\text{m}$) (SPEC Inc.) aerosol and cloud droplet size distributions for quantification of cloud liquid water content (LWC), N_d , and aerosol number concentrations with D_p exceeding $3 \mu\text{m}$ in cloud-free air (termed FCDP-aerosol); Two Dimensional Stereo (2DS; $D_p \sim 28.5 - 1464.9 \mu\text{m}$) (SPEC Inc.) probe for estimation of rain water content (RWC) by integrating raindrop ($D_p \geq 39.9 \mu\text{m}$) size distributions; Cloud Condensation Nuclei (CCN; DMT) counter for CCN number concentrations; Laser Aerosol Spectrometer (LAS; TSI Model 3340) and Condensation Particle Counter (CPC; TSI model 3772) for aerosol number concentrations with D_p between $0.1 - 1 \mu\text{m}$ and above 10 nm , respectively; High-Resolution Time-of-Flight Aerosol Mass Spectrometer (AMS; Aerodyne) for submicrometer non-refractory aerosol composition (DeCarlo et al., 2008), operated in 1 Hz Fast-MS mode and averaged to 25-second time resolution; Turbulent Air-Motion Measurement System (TAMMS) for winds and temperature (Thornhill et al., 2003).

CCN, LAS, CPC, and AMS data were collected downstream of an isokinetic double diffuser inlet (BMI, Inc.), whereas the AMS and LAS also sampled downstream of a counterflow virtual impactor (CVI) inlet (BMI, Inc.) when in cloud (Shingler et al., 2012). However, a filter was applied to remove LAS data when the CVI inlet was used. Measurements from the CCN counter, LAS, CPC, and FCDP-aerosol are only shown in cloud-free and rain-free conditions, distinguished by $\text{LWC} < 0.05 \text{ g m}^{-3}$ and $\text{RWC} < 0.05 \text{ g m}^{-3}$, respectively, and also excluding data collected 20 seconds before and after evidence of rain or cloud. Estimation of submicrometer-permicrometer-supermicrometer particles from FCDP measurements were as performed after conducting the following additional screening steps to minimize cloud droplet artifacts: (i) only samples with $\text{RH} < 98\%$ were included, (ii) data collected during ACB and BCT legs were excluded. CCN, LAS, CPC, and AMS measurements are reported at standard temperature and pressure (i.e., 273 K and 101.325 kPa (torr)) while FCDP and 2DS measurements correspond to ambient conditions.

2.3 Regression Analyses

Regression modeling was conducted to investigate relationships between environmental variables and N_d . The Gradient Boosted Regression Trees (GBRT) model, classified as a machine learning (ML) model, is used, consisting of several weak learners (i.e., regression trees with a fixed size) that are designed and subsequently trained to improve prediction accuracy by fitting the model's trees on residuals rather than response values (Hastie et al., 2009). Desirable characteristics of the GBRT model include both its capacity to capture non-linear relationships and being less vulnerable to overfitting (Persson et al., 2017; Fuchs et al., 2018; Dadashazar et al., 2020). Two separate GBRT models were trained using daily CERES-MODIS N_d data ($1^\circ \times 1^\circ$) in winter (DJF) and summer (JJA) to reveal potential variables impacting N_d . Winter and summer are chosen as they exhibit the highest and lowest N_d concentrations, respectively, among all seasons over the WNAO.

Many variables were picked as input parameters (Table 2) for the GBRT model, categorized as either being aerosol, dynamic/thermodynamic, or cloud variables. Aerosol parameters included MERRA-2 surface mass concentrations for sulfate, sea-salt, dust, and organic carbon. Black carbon concentration was removed from input parameters because of its high correlation ($R^2 = 0.6$) with organic carbon. The following is the list of thermodynamic/dynamic input parameters derived from MERRA-2: vertical pressure velocity at 800 hPa (w_{800}), planetary boundary layer height (PBLH), cold-air outbreak (CAO) index, [wind speed and wind direction at 2 m \(\$wind_{2m}\$ and \$wind-dir_{2m}\$ \)](#), relative humidity (RH) in the PBL and free troposphere represented by RH_{950} and RH_{800} , respectively. CAO index is defined as the difference between skin potential temperature (θ_{skt}) and air potential temperature at 850 hPa (θ_{850}) (Papritz et al., 2015). [Updraft speed/velocity plays a crucial role in the activation of aerosol into cloud droplets in the warm clouds \(Feingold, 2003; Reutter et al., 2009\). Since the direct representation of updraft speed is not available from reanalysis data, the near-surface wind speed \(i.e., \$wind_{2m}\$ \) is used as a representative proxy parameter here as an input parameter of the regression models, can be viewed as a proxy for the level of turbulence and also updraft speed in the marine boundary layer.](#) CERES-MODIS cloud parameters include liquid cloud fraction and cloud top height for low-level clouds. In addition, PERSIANN-CDR daily precipitation (Rain) was included as a relevant cloud parameter.

Data were split into two sets: training/validation (70%) and testing (30%). Five-fold cross-validation was implemented to train the GBRT model using the training/validation data. Furthermore, both performance and generalizability of the trained models were tested via the aid of the test set, which was not used in the training process. [The hyperparameters of the GBRT models were optimized through the combination of both random and grid search methods. Table S1 shows the list of important hyperparameters of the GBRT model and associated ranges tested via random and grid search methods. The optimized model hyperparameters can also be found in Table S1.](#) The GBRT models were performed using the scikit-learn module designed in Python (Pedregosa et al., 2011).

Table 2: List of input parameters used as predictor variables in the GBRT and linear models. Variables are grouped into three general categories.

Parameter	
Aerosol	Sulfate surface mass concentration ($\text{Sulfate}_{\text{sf-mass}}$)
	Sea-salt surface mass concentration ($\text{Sea-salt}_{\text{sf-mass}}$)
	Dust surface mass concentration ($\text{Dust}_{\text{sf-mass}}$)
	Organic carbon surface mass concentration ($\text{OC}_{\text{sf-mass}}$)
Cloud	Low-level liquid cloud fraction ($\text{CF}_{\text{low-liq.}}$)
	Low-level liquid cloud-top effective height ($\text{Cloud-top}_{\text{low-liq.}}$)
	Precipitation rate (Rain)
Dynamic/ Thermodynamic	Cold-air outbreak index ($\text{CAO}_{\text{index}}$): $\theta_{\text{skt}}^* - \theta_{850}$
	Relative humidity at 950 hPa (RH_{950})
	Relative humidity at 800 hPa (RH_{800})
	Vertical pressure velocity at 800 hPa (ω_{800})
	Wind speed at 2 m ($\text{Wind}_{2\text{m}}$)
	Wind direction at 2 m ($\text{Wind-dir}_{2\text{m}}$)
	Planetary boundary layer height (PBLH)

Parameter	
Aerosol	Sulfate surface mass concentration ($\text{Sulfate}_{\text{sf-mass}}$)
	Sea-salt surface mass concentration ($\text{Sea-salt}_{\text{sf-mass}}$)
	Dust surface mass concentration ($\text{Dust}_{\text{sf-mass}}$)
	Organic carbon surface mass concentration ($\text{OC}_{\text{sf-mass}}$)
Cloud	Low-level liquid cloud fraction ($\text{CF}_{\text{low-liq.}}$)
	Low-level liquid cloud-top effective height ($\text{Cloud-top}_{\text{low-liq.}}$)
	Precipitation rate (Rain)
Dynamic/ Thermodynamic	Cold-air outbreak index ($\text{CAO}_{\text{index}}$): $\theta_{\text{skt}}^* - \theta_{850}$
	Relative humidity at 950 hPa (RH_{950})
	Relative humidity at 800 hPa (RH_{800})
	Vertical pressure velocity at 800 hPa (ω_{800})
	Planetary boundary layer height (PBLH)

*Skin potential temperature

The regression analyses were not performed solely to construct and provide a highly accurate model useful for prediction, but rather to disclose and examine the possible effects of the relevant input variables on N_d considering all the shortcomings of such analyses. For instance, there is some level of interdependency between input variables. To reduce unwanted consequences of correlated features, the interpretation of the results was done with the aid of accumulated local effect (ALE) plots, which are specifically designed to be unbiased to the correlated input variables (Apley and Zhu, 2020). ALE plots illustrate the influence of input variables on the response parameter in ML models. The ALE value ~~of for a particular feature-variable~~ S at a specific value of x_s (i.e., $f_{s,\text{ALE}}(x_s)$) can be calculated as follows:

Formatted: Centered

$$f_{s,ALE}(x_s) = \int_{z_{0,1}}^{x_s} \int_{x_c} f^s(z_s, x_c) P(x_c|z_s) dx_c dz_s - \text{constant} \quad (2)$$

where $f^s(z_s, x_c)$ is the gradient of model's response with respect to variable S (i.e., local effect) and $P(x_c|z_s)$ is the conditional distribution of x_c where C denotes the other input variables rather than S (input features rather than S) and x_c is the associated point in the variables space of C. $z_{0,1}$ is chosen arbitrarily below the smallest observation of feature S (Apley and Zhu, 2020). The steps in Eq. 2 can be summarized as follows (Molnar, 2019; Apley and Zhu, 2020): (i) the average change in the model's prediction is calculated using the conditional distribution of features; (ii) the average change will then be accumulated by integrating it over feature S; and (iii) a constant will be subtracted to vertically center (i.e., the average of ALE becomes zero) the ALE plot. The aforementioned steps, although seemingly complex, assure the avoidance of undesired extrapolation (especially an issue for correlated variables) occurring in alternative approaches such as partial dependence (PD) plots. The value of $f_{s,ALE}(x_s)$ can be viewed as the difference between the model's response at x_s and the average prediction. We used the source code available in <https://github.com/blent-ai/ALEPython> for the calculation of ALE plots.

3. Results and Discussion

3.1 Aircraft Case Study of N_d Gradient

ACTIVATE Research Flight 5 (RF05) on 22 February 2020 demonstrates the wide range in N_d offshore in the PBL ($\lesssim 1.6$ km) over the WNAO (Figure 1). On this day, the ACTIVATE study region was dominated by a surface high pressure system centered over the southeastern U.S., with a significant ridge axis extending from the main high to the east-northeast off the Virginia-North Carolina coast and into the WNAO. Aloft, the flight region was located in northwesterly flow behind a trough offshore. This setup led to subsidence in the region and generally clear skies, except where scattered to broken marine boundary layer clouds formed along and east of the Gulf Stream. Two day NOAA HYSPLIT (Rolph et al., 2017; Stein et al., 2015; Rolph et al., 2017) back trajectories using the "model vertical velocity" method and "REANALYSIS" meteorology data indicate air in the flight region (between 0-3 km) had wrapped around the surface high from the north and left the New England coast 12-24 hours beforehand (with a descending profile). Along the flight segment shown, winds were approximately 6 m s^{-1} , out of the north/northwest during the initial descent, Min. Alt. 1, and BCB1 legs and primarily from the northeast for the other sections of the flight. Sea surface temperatures were $6 - 9^\circ\text{C}$ near the coast during the descent and Min. Alt. 1 leg (readers are referred to Fig. 1's caption for the definition of different legs), $21 - 25^\circ\text{C}$ over the Gulf Stream during the BCB1, ACB1, and BCB2 legs, and $17 - 20^\circ\text{C}$ for the remainder of the flight segment shown. The majority of the segment was in or below the boundary layer clouds, with cloud base around $900 - 1100 \text{ m}$ and cloud top around 1750 m . Note that the initial BCB1 leg was much lower at around 460 m , likely reflecting a shallower marine boundary layer and cloud base near the much colder waters close to the coast. Static air temperature ranged between $0 - 10^\circ\text{C}$, except for the BCT1 leg where temperatures were around -2.3°C .

Formatted: Not Superscript/ Subscript

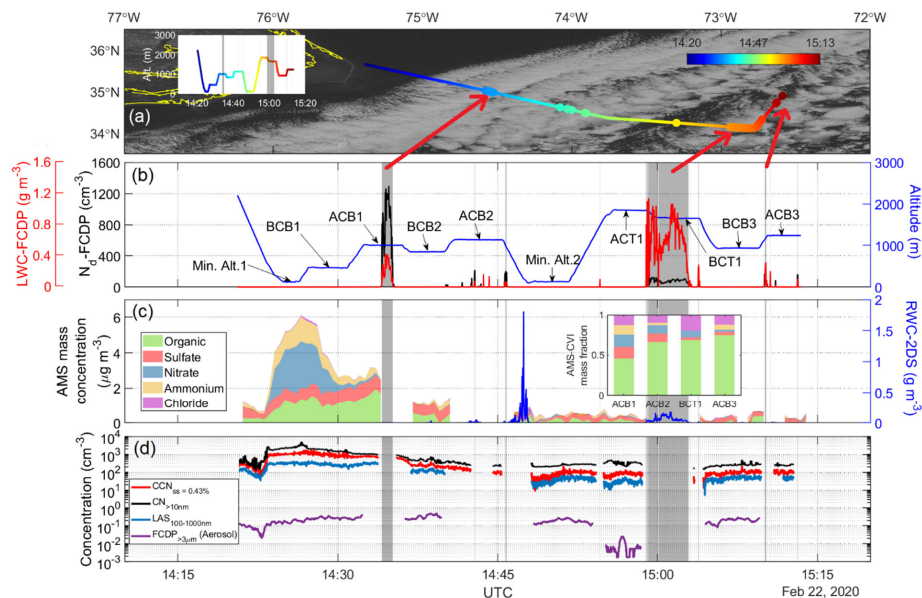


Figure 1: Time series of selected parameters measured by the HU-25 Falcon aircraft during a selected segment of RF05 on 22 February 2020: (a) overlaid flight track on GOES 16 visible imagery obtained at 14:55:04 UTC; (b) altitude, cloud liquid water content (LWC), and N_d , with the latter two obtained from the FCDP; (c) rain water content (RWC) measured by 2DS probe, AMS speciated mass concentration in cloud/rain-free air, and AMS mass fractions for droplet residual particles in cloud as measured downstream of a CVI inlet; (d) number concentrations for CCN at 0.43% supersaturation and particles for three diameter ranges: above 10 nm (CPC), 100-1000 nm (LAS), and above 3 μm (FCDP). Shaded gray areas in (b)–(d) highlight cloudy periods identified as having $\text{LWC} \geq 0.05 \text{ g m}^{-3}$. Locations of the cloudy regions are pointed to with red arrows in the satellite imagery. Level legs are defined as follows: BCB = below cloud base, ACB = above cloud base, Min. Alt. = minimum altitude the plane flies at (500 ft), ACT = above cloud top, BCT = below cloud top.

N_d values from the FCDP ranged from a maximum value of 1298 cm^{-3} closer to the coast during the ACB1 leg (35.00° N , 74.55° W) to a minimum of 19 cm^{-3} farther away in the BCT1 leg (34.32° N , 72.73° W). The minimum N_d value in the ACB3 leg was 85 cm^{-3} (34.11° N , 72.80° W), which is a fairer comparison than BCT1 leg with the ACB1 leg as compared to the BCT1 leg - in terms of being closer to cloud base. The mean N_d values (cm^{-3}) in the cloudy portions of the ACB1, BCT1, and ACB3 legs were as follows: 849, 77, 143.

Based on the nearest BCB legs adjacent to the maximum and minimum N_d values (BCB1 = 35.31° N , 74.95° W ; BCB3 = 34.41° N , 72.70° W), there was a significant offshore gradient in LAS submicrometer particle number concentration and AMS non-refractory aerosol mass, ranging from as high as 424 cm^{-3} and $5.60 \mu\text{g m}^{-3}$ (from during BCB1) to as low as 21 cm^{-3} and 0.32

$\mu\text{g m}^{-3}$ (from during BCB3), respectively; these values are based on times of the maximum and minimum LAS concentrations during the BCB1 and BCB3 legs, respectively. The mean values of submicrometer particle number concentration and AMS non-refractory aerosol for the two BCB legs were as follows: $277 \text{ cm}^{-3}/3.64 \mu\text{g m}^{-3}$ (BCB1) and $48 \text{ cm}^{-3}/0.42 \mu\text{g m}^{-3}$ (BCB3). The higher N_d value (1298 cm^{-3}) relative to LAS aerosol concentration (424 cm^{-3}) at the near-shore point is suggestive of aerosol smaller than $0.1 \mu\text{m}$ activating into drops. This is supported by the fact that both CCN (supersaturation = 0.43%) and CPC number concentrations with $D_p > 10 \text{ nm}$ exhibited mean values of 980 and 1723 cm^{-3} in the BCB1 leg, respectively, dropping to 98 and 260 cm^{-3} in the BCB3 leg. There was a slighter gradient in particle concentrations with $D_p > 3 \mu\text{m}$ (most likely sea salt) between the same two points of maximum and minimum LAS concentration in BCB1 and BCB3 legs, respectively: 0.26 cm^{-3} to 0.11 cm^{-3} . For the duration of the flight portion shown in Figure 1, supermicrometer concentrations varied over two orders of magnitude ($0.002 - 0.51 \text{ cm}^{-3}$) and expectedly did not exhibit a pronounced offshore gradient as it is naturally emitted from the ocean. Sea salt is not expected to follow the same offshore gradient as continentally derived pollution outflow.

Closer to shore during the Min. Alt. 1 leg, nitrate was the dominant aerosol species ($\sim 70\%$ mass fraction). Farther offshore during both the BCB1 leg and cloud-free portion of the ACB1 leg, organics were the dominant constituent ($\sim 46\%$ mass fraction), whereas farther during the BCB3 leg, the mean mass fraction of sulfate was the highest (75%). Droplet residual particle data show a greater contribution of organics farther offshore, increasing from 46% to 75% between the ACB1 and ACB3 legs, respectively. These composition results, albeit limited to the non-refractory portion of submicrometer aerosol particles, reveal significant changes with distance offshore indicative of varying chemical properties of particles activating into droplets.

The cloudy portions of ACB1 are characterized as having little or no rain with maximum RWC value of 0.02 g m^{-3} and mean value of 0.003 g m^{-3} . There is a notable RWC peak at the beginning of the Min. Alt. 2 leg, reaching as high as 1.81 g m^{-3} associated with clouds aloft. The precipitation occurrence was also evident in a subsequent BCT1 leg where RWC reached as high as 0.18 g m^{-3} . GOES satellite imagery of the study region (Fig. 1) also reflects the effect of precipitation on cloud morphology where clouds farther offshore resemble open-cell structures. Associated scavenging of particles through the washout process is presumed to contribute to the decline in aerosol concentrations with distance offshore.

Figure 1 shows changes in aerosol characteristics coincident with the large gradient in N_d . While ACTIVATE airborne data collection is ongoing to build flight statistics over multiple years, the wide changes in microphysical properties in RF05 motivate looking at other datasets with broader spatiotemporal coverage to learn about potential seasonally-dependent drivers of N_d , including meteorological parameters that vary throughout the year. Furthermore, other datasets can provide insight into the source(s) of seasonal discrepancy between columnar aerosol remote sensing parameters and N_d .

3.2 Seasonal Cycles of N_d and AOD

Figure 2 illustrates the seasonal differences in MERRA-2 AOD and CERES-MODIS N_d over the WNAO that partly motivate this study. Seasonal mean values (\pm standard deviation) of AOD/ N_d (cm^{-3}) were as follows for the entire WNAO: DJF = $0.11 \pm 0.03/64.1 \pm 18.0$; MAM = $0.16 \pm 0.03/60.4 \pm 13.1$; JJA = $0.15 \pm 0.03/49.1 \pm 10.1$; SON = $0.11 \pm 0.03/50.3 \pm 13.9$. In contrast to AOD, N_d values and low-cloud fraction (Figure 2c) were highest in DJF and lowest in JJA. DJF showed notably high N_d near the coast, qualitatively consistent with the airborne data. The seasons

with the greatest AOD values, accompanied by the most pronounced spatial gradient offshore, were JJA and MAM. The offshore gradient owes to continental pollution outflow (Corral et al., 2021 and references therein). In contrast, DJF and SON exhibited lower AOD values with a distinct area of higher AOD values offshore between $\sim 35^\circ - 40^\circ$ N accounted for by sea salt. MERRA-2 speciated AOD data (Figure S43) indicate that sea salt and sulfate dominate total AOD regardless of season and that sulfate, organic carbon, and black carbon most closely follow the offshore gradient pattern owing to continental sources. Dust and sea salt have different spatial distributions with the former derived from sources such as North Africa leading to enhanced AODs $< 30^\circ$ N especially in JJA, and sea salt being enhanced offshore especially in JJA.

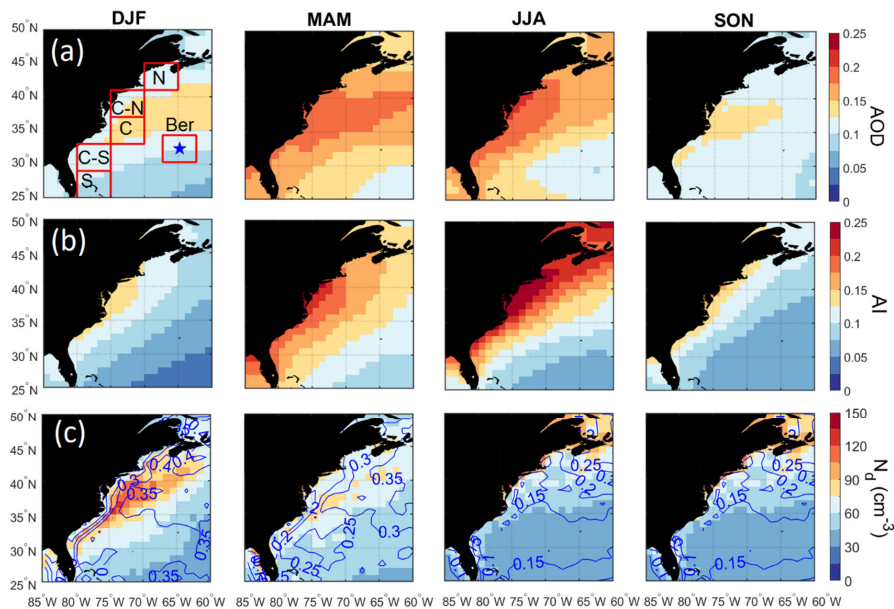


Figure 2: Seasonal spatial maps for (a) MERRA-2 aerosol optical depth (AOD), (b) MERRA-2 aerosol index (AI), and (c) cloud drop number concentration (N_d) over the western North Atlantic Ocean (WNAO). Contours in (c) represent low-level (cloud top pressure > 700 hPa) liquid cloud fraction ($CF_{low-liq.}$). Cloud data are based on daily Level 3 data from CERES-MODIS. The maps are based on data between January 2013 and December 2017. The boxes in top left panel represent sub-domains examined in more detail throughout the study, with the blue star denoting Bermuda.

Table 3 probes deeper into individual WNAO sub-domains to compare seasonal AOD and N_d values. For the six sub-domains in Figure 2, MERRA-2 AOD peaks in MAM and JJA, while N_d peaks in DJF. The Bermuda sub-domain was unique in that mean N_d was slightly higher in MAM (53 cm^{-3}) as compared to DJF (48 cm^{-3}). We attribute the slightly different seasonal cycle

432 over Bermuda to its remote nature leading to differences in meteorology and aerosol sources
433 between seasons.

434 One factor that could bias AOD towards higher values with disproportionately less impact
435 on N_d is aerosol hygroscopic growth in humid conditions. Table 3 summarizes mean MERRA-2
436 RH values in the PBL and free troposphere (FT). Results show that while RH is highest in JJA
437 (except for FT of DJF in sub-domain N), differences between seasons were not very large. The
438 maximum difference among the four seasons when considering mean RH in the PBL and FT for
439 all sub-domains ranged between 3% – 9% and 7% – 25%, respectively. Consequently, humidity
440 effects on remotely sensed aerosol parameters ~~cannot~~ is are less likely to be sole explanation
441 of alone explain the dissimilar seasonal cycle of N_d and AOD, but can plausibly contribute to some
442 extent.

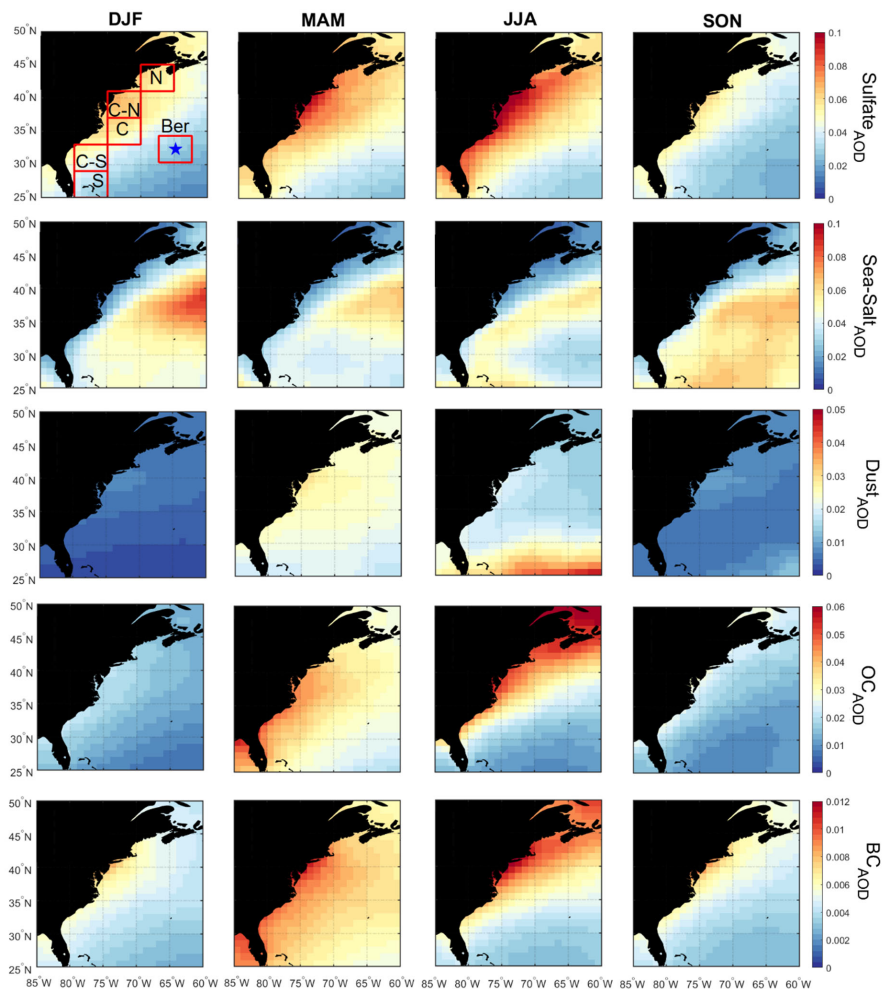


Figure 3: Seasonal maps of MERRA-2 speciated AOD based on data between January 2013 and December 2017. The boxes in top left panel represent sub-domains examined in more detail throughout the study, with the blue star denoting Bermuda.

One factor that could drive the seasonal variation in N_d is the unwanted effects of retrieval errors in the estimation of N_d at low cloud coverage conditions. It is shown that the uncertainty associated with the estimation of N_d from MODIS observation increases as cloud fraction decreases (Grosvenor et al., 2018). This is mainly because of the overestimation of droplet effective radius (r_e) in the retrieval algorithm due to the interference of cloud-free pixels and also

Formatted: Centered

Formatted: Indent: First line: 0.5"

Formatted: Subscript

high spatial inhomogeneity in low cloud coverage conditions that violates horizontal homogeneity assumptions in the retrieval of r_e and τ from radiative transfer modeling (Zhang et al., 2012; Zhang et al., 2018). To test whether retrieval errors in N_d are the main driver of seasonal trends, Figure S1 was constructed which exhibits the seasonal cycle of N_d at various low-level liquid cloud fractions. The results presented in Fig. S2 show that as cloud fraction increases the average N_d increases, regardless of season. Perhaps, but the more important finding is that the seasonal trend in spatial maps of N_d remains similar regardless of cloud fraction. This finding is important as it confirms that the seasonal cycle in N_d cannot be solely explained by the uncertainties associated with the retrieval of N_d at low cloud fraction.

3.3 Contrasting AOD and Aerosol Index

While previous studies have pointed to the limitations of AOD as an aerosol proxy (e.g., Stier, 2016; Gryspeerdt et al., 2017; Painemal et al., 2020), the N_d -AOD anticorrelation at seasonal scale over the WNAO is at odds with findings for other regions supporting the relationship between these two parameters (Quaas et al., 2008; Sekiguchi et al., 2003; Nakajima et al., 2001; Sekiguchi et al., 2003; Quaas et al., 2006; Quaas et al., 2008; Grandey and Stier, 2010; Penner et al., 2011; Gryspeerdt et al., 2016; Grandey and Stier, 2010) and also that between sulfate and N_d (Boucher and Lohmann, 1995; Lowenthal et al., 2004; Storelvmo et al., 2009; McCoy et al., 2017; McCoy et al., 2018; MacDonald et al., 2020; McCoy et al., 2017; MacDonald et al., 2020; McCoy et al., 2018; Storelvmo et al., 2009; Lowenthal et al., 2004; Boucher and Lohmann, 1995). Values of N_d are influenced by the number concentration of available CCN, which is determined by aerosol properties (size distribution and composition) and supersaturation level. AOD is an imperfect CCN proxy variable because it does not provide information about composition and size distribution, and is sensitive to relative humidity. Aerosol index (AI) is more closely related to CCN as it partially accounts for the size distribution of aerosols (Deuze et al., 2001; Nakajima et al., 2001; Deuze et al., 2001; Breon et al., 2002; Hasekamp et al., 2019). The sensitivity of AI to size is evident in spatial maps for each season showing more of an offshore gradient (like sulfate AOD in Figure S43) in each season and lacking both the offshore peak in sea salt between $\sim 35^\circ - 40^\circ$ N and the maximum AOD for dust south of 30° N in JJA. However, when comparing absolute values between the four seasons in Figure 2b, AI exhibits a similar seasonal cycle as AOD, thereby indicating that size distribution alone cannot explain diverging seasonal cycles for N_d and AOD. We next compare N_d to aerosol data in the PBL where CCN more relevant to droplet activation are confined. Size distribution effects in the PBL can instead be more of a factor especially as sea salt is abundant.

3.4 Aerosol Size Distribution and Vertical Aerosol Distribution

Vertical profiles of aerosol extinction coefficient estimated from CALIOP nighttime observations are shown in Figure 3-4 for the six sub-domains. Shown also are the seasonally representative planetary boundary layer heights (PBLHs) from MERRA-2, with numerical values of both PBLH and fractional AOD contributions to the PBL and FT in Table 3. Although here we used nighttime observations from CALIOP because of having higher signal to noise ratio than daytime observations, we expect the general seasonal trends discussed here to remain the same regardless of the observation time. The CALIOP results indicate that aerosol extinction more closely follows the N_d seasonal cycle with the highest (lowest) values in the PBL during DJF (JJA). However, aerosol extinction coefficient is sensitive to aerosol size distribution and a plausible scenario is that DJF extinction in the PBL is primarily contributed by coarse sea salt particles,

Formatted: Font: (Default) +Headings CS (Times New Roman), 12 pt, Font color: Text 1, Complex Script Font: +Headings CS (Times New Roman), 12 pt, Bold

Formatted: Subscript

which are especially hygroscopic, but do not contribute significantly to number concentration as demonstrated clearly by airborne observations (i.e., FCDP_{>3μm} time series shown in Figure 1d). This is supported in part by how DJF is marked by the highest fractional AOD contribution from the PBL (59 – 72%) where sea salt is concentrated. In contrast, JJA has the lowest fractional AOD contribution from the PBL (11.3 – 52.6%). It is also possible that the higher contribution of higher fractional AOD contribution from the PBL to AOD in winter than summer partly owes to be the results of more number of aerosol particles being more strongly trapped in confined to the PBL in DJF as compared to the summer. Sub-domains C-N and N exhibit the greatest changes in AOD fraction in the PBL between seasons with a maximum in DJF (59 – 61%) and a minimum in JJA (11 – 19%) suggesting they are relatively more sensitive to the aerosol vertical distribution in leading to contrasting AOD and N_a seasonal cycles. Bermuda stands out as having the highest AOD fractional contributions in the PBL in DJF (72%) and SON (69%) and among the highest seasonal total AODs in those two seasons (0.14 in DJF and 0.10 in SON) assisted in large part from sea salt (Figure S43) (Aldhaif et al., 2021), coincident with high seasonal wind speeds (Corral et al., 2021).

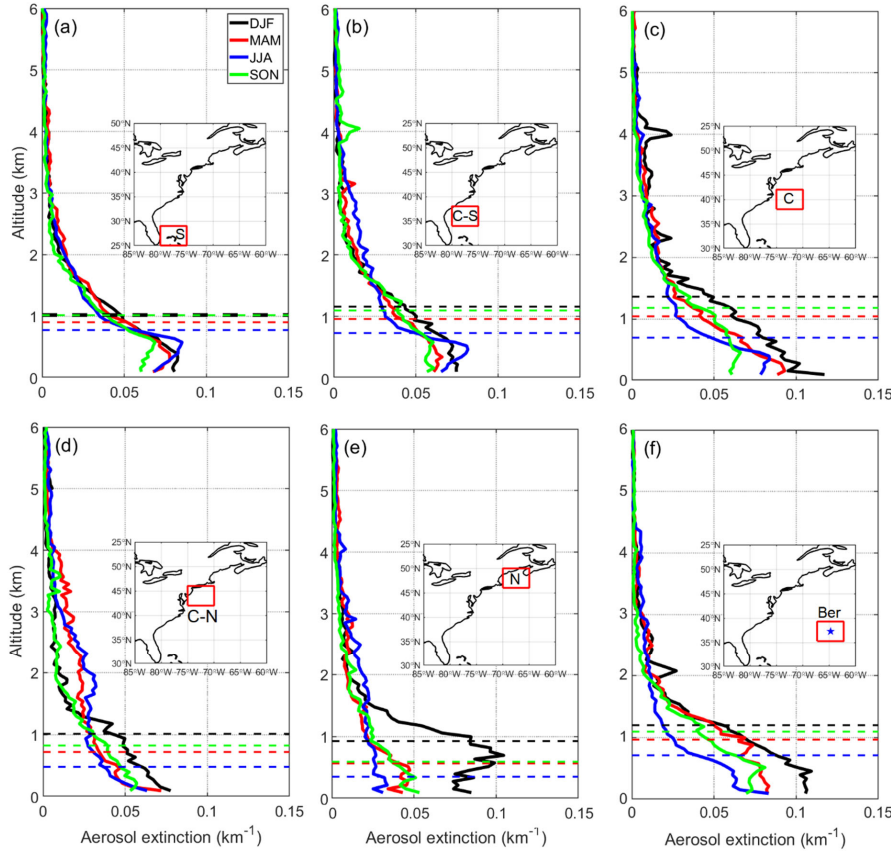


Figure 34: Vertical profiles of CALIPSO aerosol extinction for different seasons in (a-f) six different sub-domains of the WNAO. Average seasonal planetary boundary layer heights (PBLH) from MERRA-2 are denoted with dashed lines.

To explore aerosol number concentration characteristics in the PBL in different seasons, we next discuss results from an opportune dataset over the U.S. East Coast (Cape Cod, MA) providing an annual profile of CCN concentration at 1% supersaturation (Figure 45). Cape Cod is a coastal location representative of the outflow providing an important fraction of the CCN impacting offshore low-level clouds. As the supersaturation examined is relatively high (1%), the measured CCN include smaller particles representing high number concentrations that would not appreciably contribute to the high aerosol extinctions from CALIOP in the PBL in direct contrast to sea salt (i.e., high extinction due to fewer but larger particles). Seasonal mean CCN values do not follow the seasonal cycle of N_d nor CALIOP extinction in the PBL, with values being as follows: DJF =

1436 cm⁻³; MAM = 1533 cm⁻³; JJA = 1895 cm⁻³; SON = 1326 cm⁻³. These results suggest the following: (i) size distribution effects are significant in the PBL when comparing extinction to number concentration; and (ii) aerosol vertical distribution behavior cannot alone explain the divergent seasonal cycles of N_d and aerosol parameters (e.g., AOD, AI, surface number concentrations).

Table 3: Average drop number concentration (N_d), MERRA-2 AOD, and vertically resolved AOD characteristics from CALIOP for each season over the sub-domains shown in Figure 2. Total CALIOP AOD is shown outside parentheses and numbers inside are the percent AOD fraction in the planetary boundary layer followed by in the free troposphere. Also shown are PBLHs (shown in Figure 34) and the relative humidity in the PBLH and FT.

	AOD _{MERRA-2} /N _d (cm ⁻³)					
	S	C-S	C	C-N	N	Bermuda
DJF	0.10/56	0.11/74	0.13/91	0.12/97	0.11/78	0.10/48
MAM	0.14/55	0.17/62	0.18/72	0.19/75	0.16/70	0.14/53
JJA	0.14/41	0.16/43	0.17/47	0.19/68	0.17/73	0.11/37
SON	0.11/42	0.12/53	0.13/62	0.13/74	0.11/73	0.11/36
	AOD _{CALIOP} (%PBL,%FT)					
	S	C-S	C	C-N	N	Bermuda
DJF	0.11 (64,36)	0.11 (67,33)	0.15 (68,32)	0.09 (61,39)	0.13 (59,41)	0.14 (72,28)
MAM	0.11 (54,46)	0.10 (53,47)	0.12 (58,42)	0.10 (30,70)	0.07 (30,70)	0.12 (58,42)
JJA	0.11 (53,47)	0.11 (44,56)	0.10 (46,54)	0.11 (20,80)	0.08 (11,89)	0.08 (49,51)
SON	0.09 (63,37)	0.10 (57,43)	0.10 (65,35)	0.08 (47,53)	0.07 (35,65)	0.10 (69,31)
	PBLH (m)/RH _{PBL} (%)/RH _{FT} (%)					
	S	C-S	C	C-N	N	Bermuda
DJF	1018/78/37	1156/76/43	1364/79/46	1013/76/52	926/76/58	1198/80/43
MAM	903/77/41	955/72/43	1043/75/48	722/72/53	568/79/55	966/79/50
JJA	775/81/62	725/81/60	697/81/59	481/78/53	351/85/55	713/82/58
SON	1018/80/50	1094/76/45	1181/76/42	825/71/43	593/77/51	1095/81/48

We next compare MERRA-2 speciated aerosol concentrations at the surface (Figure 6S2) to those of speciated AOD (Figure S43). Surface mass concentrations have the limitation of being biased by larger particles (similar to extinction). The seasonal cycle of mean values for speciated AOD and surface concentration for individual sub-domains generally agree with the exception that there was disagreement for sulfate in each sub-domain (see seasonal mean values in Table S2+). Sulfate exhibited higher AODs in JJA but with surface concentrations usually highest in DJF or MAM; although differences in seasonal mean mass concentrations were relatively small (< 1 µg m⁻³), a plausible explanation is enhanced secondary production of sulfate via oxidation of SO₂ or DMS convectively lifted to the free troposphere in JJA. An important result confirmed by the surface mass concentrations is that sea salt is an order of magnitude higher than the other species, supporting the previous speculation that sea salt dominates the aerosol extinction in the PBL from CALIOP.

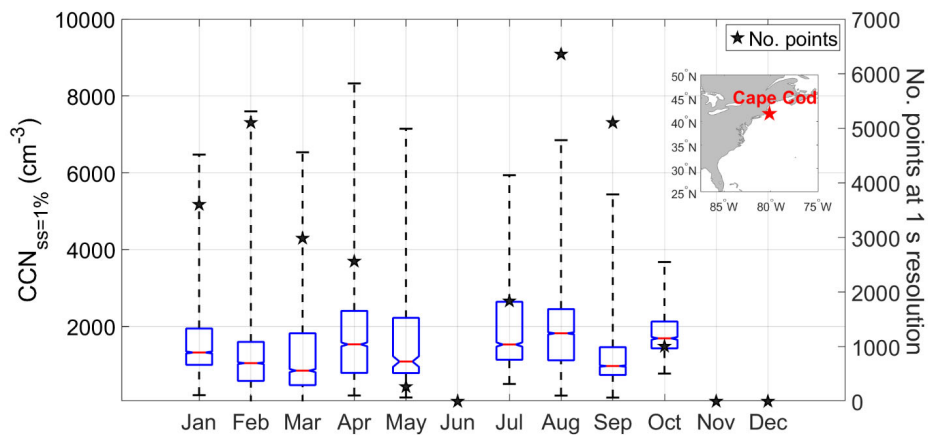


Figure 45: Monthly statistics of CCN concentration (1% supersaturation) measured at Cape Cod between July 2012 and May 2013. Red lines represent median, whiskers are the monthly range, and the top and bottom of boxes represent the 75th and 25th percentile, respectively. The notches in the box plots demonstrate whether medians are different from each other with 95% confidence. Boxes with notches that do not overlap with each other have different medians with 95% confidence.

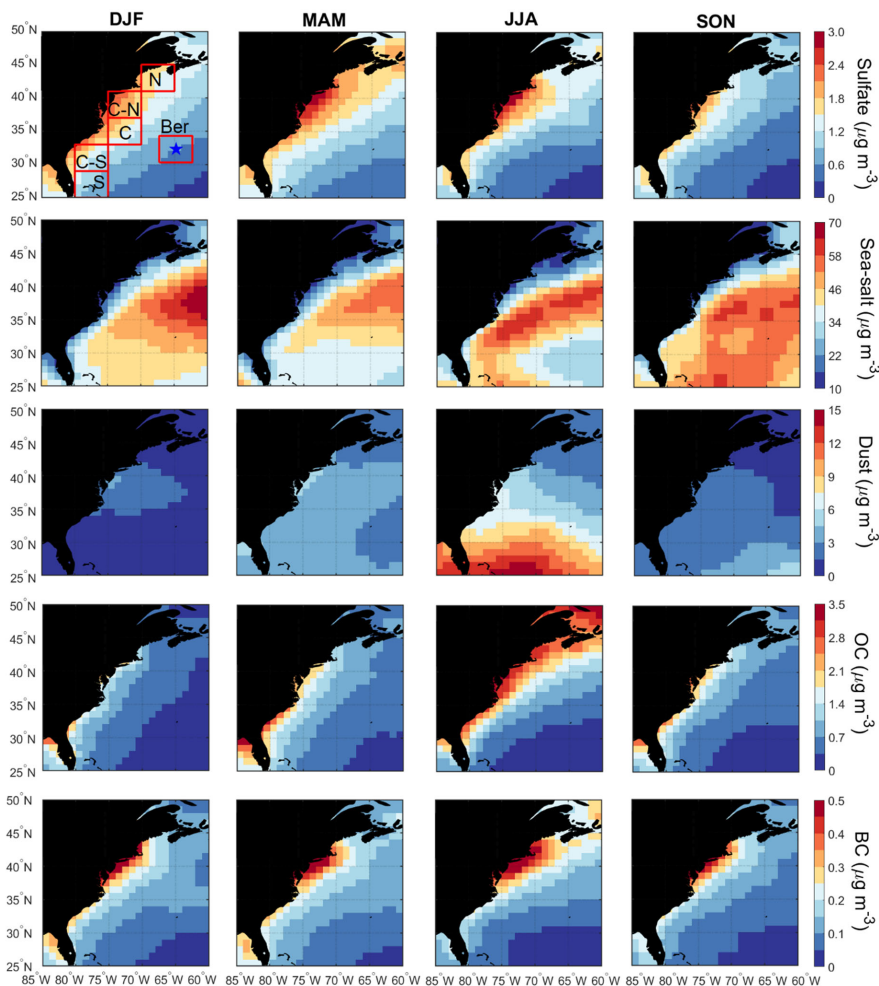


Figure 6: Seasonal maps MERRA-2 speciated aerosol concentrations at the surface, based on data between January 2013 and December 2017. The boxes in top left panel represent sub-domains examined in more detail throughout the study, with the blue star denoting Bermuda.

Formatted: Centered

Formatted: Font: (Default) Times New Roman, Bold, Font color: Auto, Complex Script Font: Times New Roman, Do not check spelling or grammar

Formatted: Font: (Default) Times New Roman, Font color: Auto, Complex Script Font: Times New Roman

3.5 Aerosol-Cloud Interactions

Studies of China's east coast have shown that the aerosol indirect effect is especially strong in wintertime, whereby pollution outflow leads to high Na and suppressed precipitation (Berg et

al., 2008; Bennartz et al., 2011). It is hypothesized that a similar effect is taking place off of North America's east coast, which could in part explain enhanced N_d without necessarily a significant jump in aerosol parameter (e.g., AOD, AI) values. Grosvenor et al. (2018) suggested that high cloud fractions in wintertime off these east coasts relative to other seasons are coincident with strong temperature inversions usually associated with cold air outbreaks that serve to concentrate and confine surface layer aerosols. We examine the relative seasonal strength of the aerosol indirect effect via spatial maps of the following metric commonly used in aerosol-cloud interaction (ACI) studies:

$$ACI = d\ln(N_d)/d\ln(\alpha) \quad (3)$$

where α represents an aerosol proxy parameter that is represented here as AI, AOD, the speciated sulfate AOD (Sulfate_{AOD}), and sulfate surface mass concentration (Sulfate_{sf-mass}). The expected range by common convention is 0 – 1, with higher values suggestive of greater enhancement in N_d for the same increase in the aerosol proxy parameter.

Table 4 shows that DJF ~~usually~~ always exhibits the highest ACI values regardless of the aerosol proxy used, consistent with a stronger aerosol indirect effect in DJF over East Asia. The mean ACI values in DJF using AI, AOD, Sulfate_{AOD}, and Sulfate_{sf-mass} ranged from 0.25 to 0.55, 0.28 – 0.59, 0.25 – 0.53, and 0.22 – 0.47, respectively, depending on the sub-domain. Spatial maps of ACI (Figure S7) do not point to significant geographic features. Coefficients of determination (R^2), ~~for the linear regression between $\ln(N_d)$ and $\ln(\alpha)$~~ , when computing seasonal ACI values were generally low (≤ 0.30), with spatial maps of R^2 and data point numbers in Figure S3S2. Poor correlations are suggestive of the non-linear nature of aerosol-cloud interactions (e.g., Gryspeerdt et al., 2017) and the influence of other likely factors such as dynamical processes and turbulence, data spatial resolution and dataset size, cloud adiabaticity, wet scavenging effects, and aerosol size distribution (McComiskey et al., 2009). The results of this section suggest though that aerosol indirect effects could be strongest in DJF, meaning that N_d values increase more for the same increase in aerosol. Factors that can contribute to higher ACI values in winter than summer can be differences in the following conditions include seasonal differences in the following: (i) dynamical processes and turbulence structures of the marine boundary layer; (ii) aerosol size distributions and consequently different abundance in the varying particle number concentrations of aerosol for the same amount of a fixed mass concentrations; and (iii) hygroscopicity of particles especially as a result of changes in the composition of organic carbons the carbonaceous aerosol fraction. Regarding dynamical processes and the effects of turbulence, Figure 2 in Painemal et al. (2021) showed in their study (Figure 2 in their paper) that heat fluxes (i.e., including both latent and sensible fluxes) were the strongest (lowest) in the winter and the lowest in the (summer) over the WNAO. The greater heat fluxes in DJF can contribute to the more turbulent and coupled marine boundary layer conditions in winter than summer, that can in turn result presumably resulting in more efficient transport and activation of aerosol in the marine boundary layer leading to and consequently higher ACI values. Forthcoming work will probe this issue in greater detail.

Table 4: Estimated values of ACI calculated four ways ($\text{dlog}(N_d)/\text{dlog}(\text{AOD})$; $\text{dlog}(N_d)/\text{dlog}(\text{AI})$; $\text{dlog}(N_d)/\text{dlog}(\text{Sulfate}_{\text{AOD}})$; $\text{dlog}(N_d)/\text{dlog}(\text{Sulfate}_{\text{sf-mass}})$) for the sub-domains shown in Figure 2. The ACI values were obtained from log-log regression on average daily values of N_d and each of the aerosol proxy variables including only the pixels with $\text{CF}_{\text{low-liq.}}$ greater than 0.1. Numbers in parentheses, in order, are R^2 and the number of points used for linear regression. Statistically insignificant ACI values with p-value greater than 0.05 are marked by bold font.

	ACI-AI					
	S	C-S	C	C-N	N	Bermuda
DJF	0.55 (0.24,440)	0.53 (0.17,421)	0.53 (0.14,403)	0.33 (0.05,418)	0.25 (0.04,403)	0.42 (0.09,422)
MAM	0.21 (0.03,451)	0.13 (0.01,439)	0.30 (0.06,422)	0.17 (0.02,426)	0.31 (0.05,428)	0.28 (0.04,437)
JJA	0.25 (0.02,437)	0.20 (0.03,437)	0.28 (0.07,424)	0.11 (0.01,430)	-0.12 (0.01,408)	0.38 (0.09,443)
SON	0.23 (0.03,435)	0.20 (0.03,428)	0.26 (0.05,431)	0.19 (0.04,412)	0.24 (0.06,394)	0.00 (0.00,428)
all	0.27 (0.05,1763)	0.16 (0.02,1725)	0.22 (0.04,1680)	0.12 (0.01,1686)	0.12 (0.01,1633)	0.23 (0.04,1730)
	ACI-AOD					
DJF	0.59 (0.13,440)	0.53 (0.12,421)	0.47 (0.10,403)	0.39 (0.06,418)	0.28 (0.04,403)	0.37 (0.08,422)
MAM	0.26 (0.02,451)	0.22 (0.01,439)	0.43 (0.07,422)	0.30 (0.04,426)	0.40 (0.06,428)	0.32 (0.03,437)
JJA	0.02 (0.00,437)	0.24 (0.02,437)	0.36 (0.07,424)	0.15 (0.01,430)	-0.06 (0.00,408)	0.30 (0.04,443)
SON	0.14 (0.01,435)	0.18 (0.02,428)	0.17 (0.02,431)	0.16 (0.02,412)	0.27 (0.05,394)	0.18 (0.02,428)
all	0.13 (0.01,1763)	0.12 (0.01,1725)	0.22 (0.03,1680)	0.15 (0.01,1686)	0.16 (0.02,1633)	0.31 (0.05,1730)
	ACI-Sulfate _{AOD}					
DJF	0.53 (0.25,440)	0.53 (0.21,421)	0.53 (0.19,403)	0.37 (0.08,418)	0.25 (0.05,403)	0.43 (0.13,422)
MAM	0.29 (0.05,451)	0.27 (0.04,439)	0.42 (0.14,422)	0.32 (0.07,426)	0.41 (0.11,428)	0.34 (0.07,437)
JJA	0.21 (0.02,437)	0.19 (0.03,437)	0.33 (0.09,424)	0.20 (0.04,430)	0.04 (0.00,408)	0.39 (0.09,443)
SON	0.16 (0.02,435)	0.23 (0.04,428)	0.29 (0.07,431)	0.28 (0.09,412)	0.35 (0.13,394)	0.07 (0.00,428)
all	0.23 (0.04,1763)	0.19 (0.03,1725)	0.30 (0.07,1680)	0.23 (0.05,1686)	0.22 (0.05,1633)	0.25 (0.05,1730)
	ACI-Sulfate _{sf-mass}					
DJF	0.44 (0.29,440)	0.41 (0.22,421)	0.47 (0.22,403)	0.22 (0.04,418)	0.23 (0.06,403)	0.32 (0.14,422)
MAM	0.24 (0.07,451)	0.25 (0.08,439)	0.29 (0.12,422)	0.24 (0.05,426)	0.36 (0.09,428)	0.16 (0.04,437)
JJA	0.11 (0.01,437)	0.12 (0.03,437)	0.23 (0.11,424)	0.19 (0.06,430)	-0.12 (0.01,408)	0.20 (0.07,443)
SON	0.32 (0.16,435)	0.36 (0.18,428)	0.34 (0.19,431)	0.19 (0.06,412)	0.21 (0.05,394)	0.17 (0.07,428)
all	0.32 (0.13,1763)	0.30 (0.12,1725)	0.36 (0.17,1680)	0.19 (0.04,1686)	0.15 (0.02,1633)	0.25 (0.11,1730)

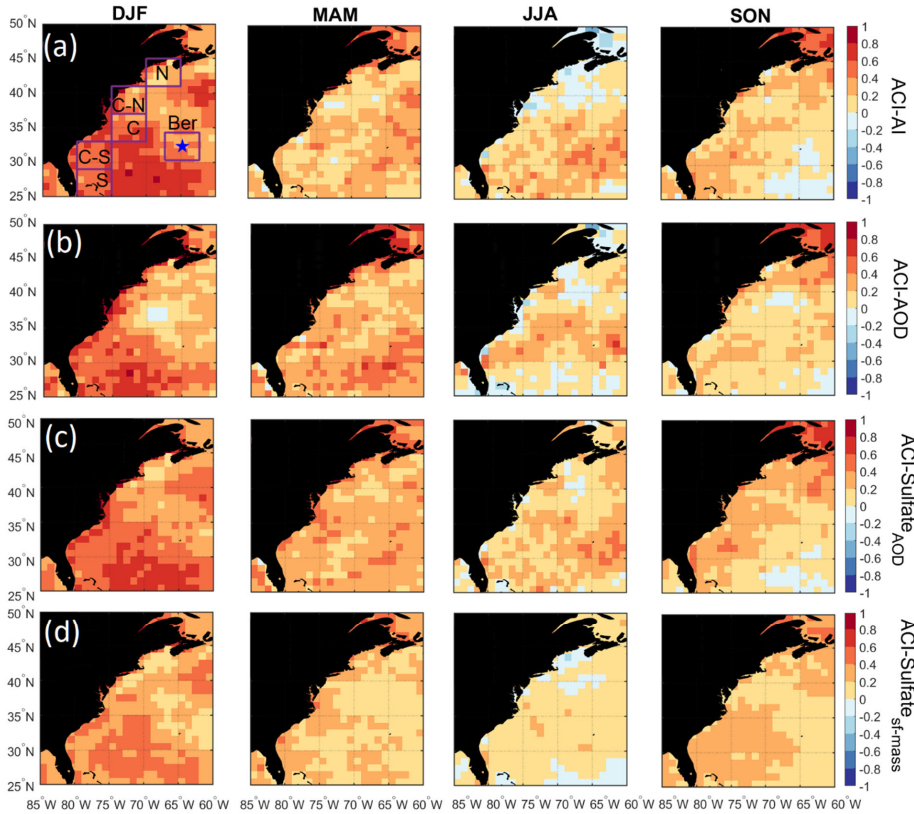


Figure 57: Seasonal maps of the aerosol-cloud interaction (ACI) parameters over the WNAO using daily N_d and four different aerosol proxy parameters (AI, AOD, Sulfate_{AOD}, Sulfate_{sf-mass}) from CERES-MODIS and MERRA-2, respectively. ACI statistics associated with the six sub-domains shown are summarized in Table 4.

4. Discussion of Potential Influential Factors

We probe deeper into factors related to the N_d seasonal cycle by using (Section 4.1) composite analyses based on “high” and “low” N_d days, and (Section 4.2) advanced regression techniques tackling non-linear relationships. We focus the analyses on one sub-domain (C-N) both for simplicity and intriguing characteristics: (i) among the highest anthropogenic AOD values over the WNAO, (ii) significant seasonal changes in fractional AOD contribution to the PBL, (iii) close to the Cape Cod site where CCN data were shown, and (iv) the aerosol indirect effect (Table 4) is strongest (weakest) in DJF (JJA).

4.1 Composite Analysis

Discussion first addresses the behavior of different environmental parameters on days with the highest and lowest N_d values. Seasonal histograms of averaged daily N_d were generated for sub-domain C-N. The histograms are based on the natural logarithm of N_d to better resemble a normal distribution. ~~Subsequently, one standard deviation from both sides of the seasonal mean defined cut-off points outside of which we~~ we assign values as being low and high in each season ~~if they are less than one standard deviation below the seasonal value; conversely, high values are those exceeding one standard deviation above the seasonal mean.~~ Cut-off N_d values (cm^{-3}) are as follows (low/high): 33/153 (DJF), 29/118 (MAM), 38/100 (JJA), and 31/115 (SON). Next, composite maps for these groups were created (Figures ~~6-8 – 1012~~) for sea level pressure, near-surface wind, low-level cloud fraction, cold-air outbreak index, and AOD. The figures contrast the low and high N_d maps with those showing mean seasonal values to investigate potential factors that contribute to seasonal N_d variability. Interested readers are referred to Figures S34 – S204 where similar composite map results are shown for N_d itself and other parameters including those in Table 2.

The resulting composite maps indicate high N_d days are characterized by (i) reduced SLP; (ii) more northerly-northwesterly flow for all seasons (except JJA) and especially stronger winds in DJF and SON; (iii) higher low-level liquid cloud fraction, especially in DJF; (iv) higher CAO index in the seasons when CAO events occur more frequently (DJF, SON, MAM); and (v) enhanced AOD. Low N_d days generally exhibited opposite conditions when compared to seasonal mean values: (i) enhanced SLP; (ii) wind ranging from southerly to westerly without any significant wind speed enhancement; (iii) reduced low-level liquid cloud fraction, especially in DJF; (iv) lower CAO index in DJF, SON, and MAM; and (v) reduced AOD in DJF and MAM, enhanced AOD in JJA, and limited change in SON. Noteworthy results from Figures S34 – S204 included the enhancement/reduction of PBLH on high/low N_d days (least pronounced in JJA), higher/lower RH at 950 and 800 hPa on high/low N_d days, and higher/lower sulfate AOD and surface concentrations on high/low N_d days for DJF and MAM. Furthermore, there was a general reduction in rain on low N_d days for most seasons except SON, with rain enhancement on high N_d days except for DJF (Figure S67); this was unexpected as wet removal was hypothesized to be a reason for reduced N_d for at least the low N_d days. This may be attributed to the rain product being for surface precipitation (and thus not capturing all drizzle) and for all cloud types, including more heavily precipitating clouds deeper and higher than the low-level clouds examined for N_d . ~~Another factor that can contributed potentially contributing to the observed counterintuitive trends is the temporal offset between N_d estimations from MODIS-Aqua and precipitation data from PERSIANN-CDR.~~

The mean seasonal climatological values and anomalies suggest that high N_d cases are marked by continental outflow, high cloud fractions, high PBLH, and low SLP, all of which occur most commonly in DJF and are associated with cold air outbreaks. These events are marked by cold air over the warm ocean leading to strong surface heat fluxes, boundary layer deepening, weakened inversion strength, in addition to high and deep clouds (Brummer, 1996; Kolstad et al., 2009; Fletcher et al., 2016; Abel et al., 2017; Brummer, 1996; Naud et al., 2018). Coincident with these features is the Icelandic Low, which is a significant climatological feature of the North Atlantic whereby subpolar low pressure builds in extratropic areas beginning in the fall with westerly winds in the boundary layer that shift more to northerly in the winter (Sorooshian et al.,

Formatted: Subscript

2020;Painemal et al., 2021). This low-pressure system seems to be stronger on high N_d days resulting in more continental outflow and high number concentrations of CCN; the greater CAO index values near the coast promote high cloud coverage affording more opportunity for cloud processing of particles to ultimately enhance droplet activation. While there can be considerable enhancement in N_d as cold air outbreak air masses evolve over warmer waters, precipitation scavenging farther downwind will be an efficient method of boundary layer aerosol (and N_d) removal (Abel et al., 2017; Lloyd et al., 2018), which contributes at least in part to the sharp N_d gradients offshore demonstrated in Figure 1.

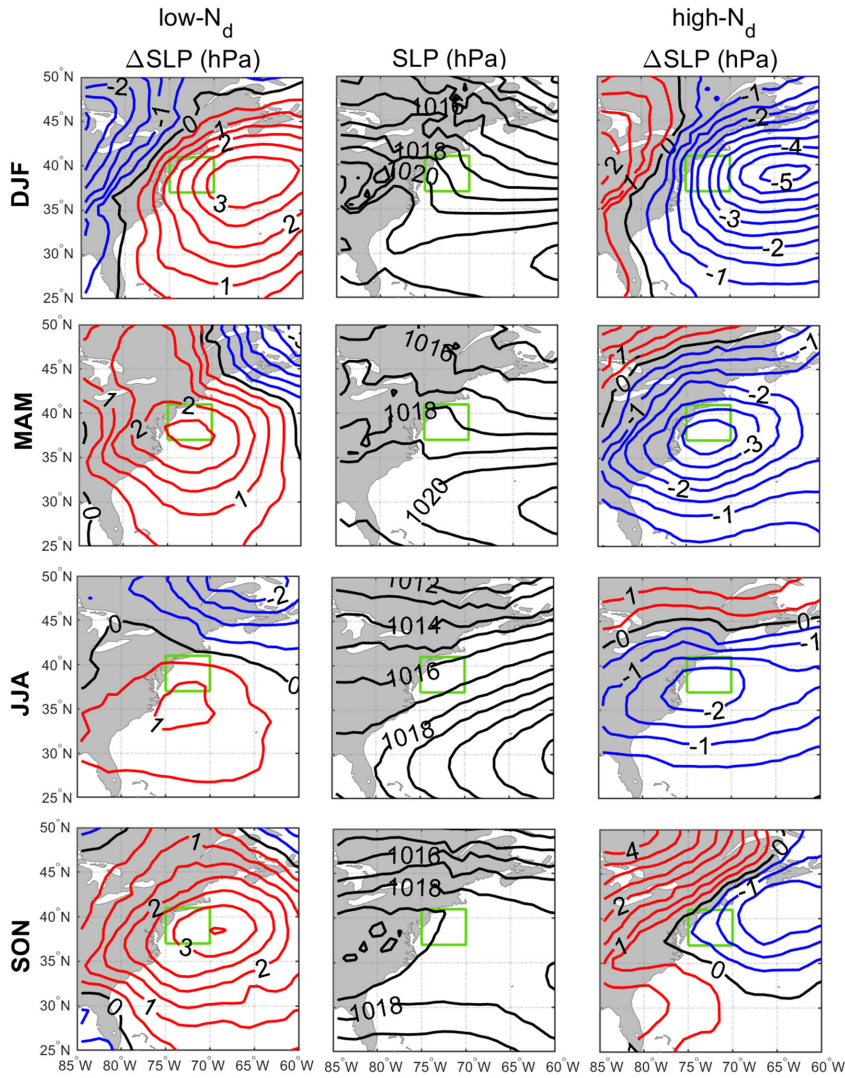


Figure 68: Seasonal climatology of sea-level pressure (SLP) (middle column) and anomalies from seasonal averages for low- N_d days (left column) and high- N_d days (right column). In the left and right columns, red and blue contours are associated with positive and negative anomalies from the climatology, respectively. The green box represents sub-domain C-N for which the analysis was conducted.

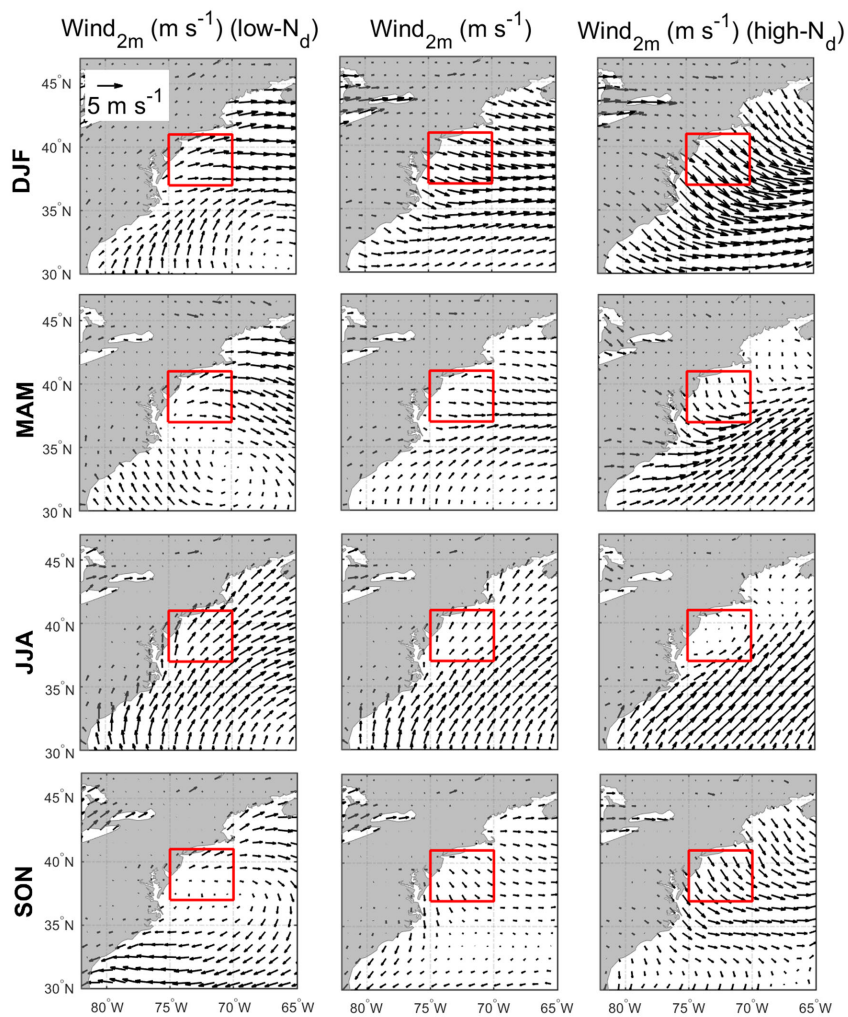


Figure 79: Seasonal climatology of near-surface (2 m above ground) wind speed (middle column) and mean values for low- N_d days (left column) and high- N_d days (right column). The reference wind vector is shown on the top left panel. The red box represents sub-domain C-N for which the analysis was conducted.

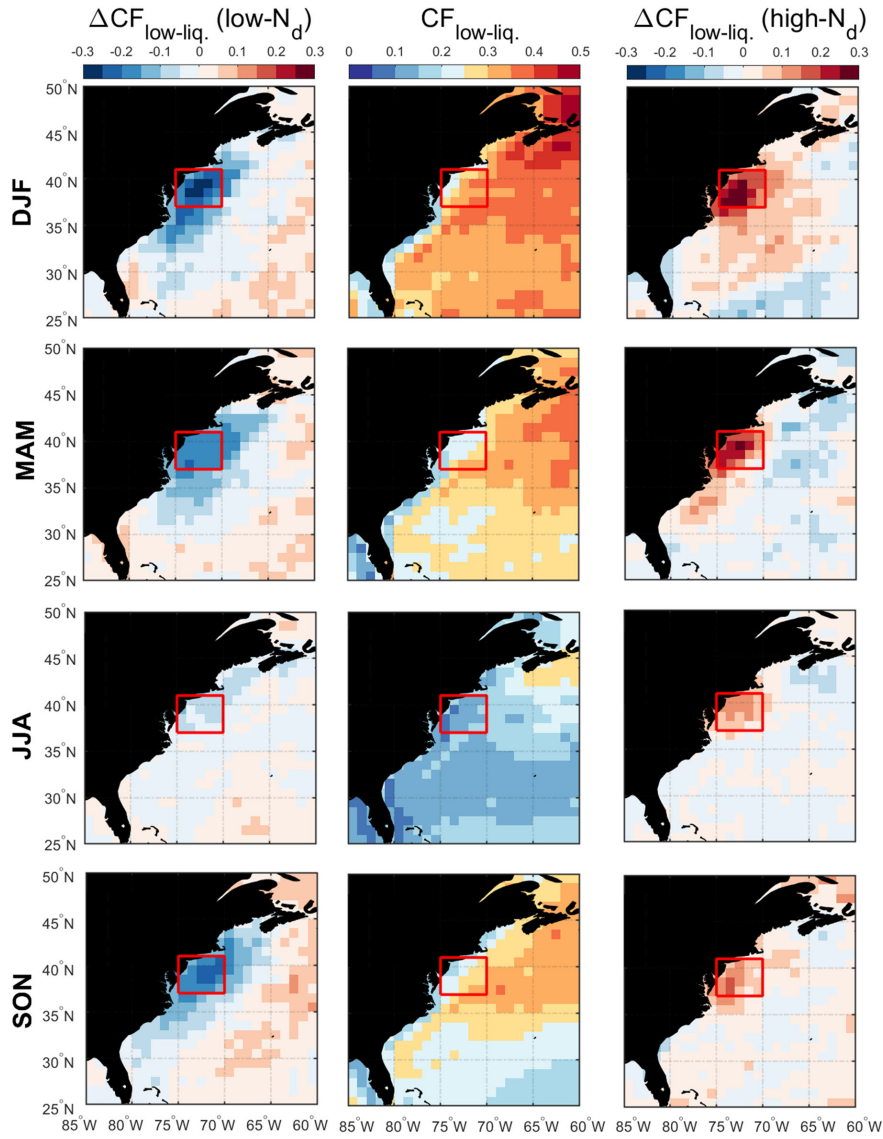


Figure 810: Seasonal averages of low-level liquid cloud fraction (middle column) and associated anomalies on low- N_d days (left column) and high- N_d days (right column). The red box represents sub-domain C-N for which the analysis was conducted.

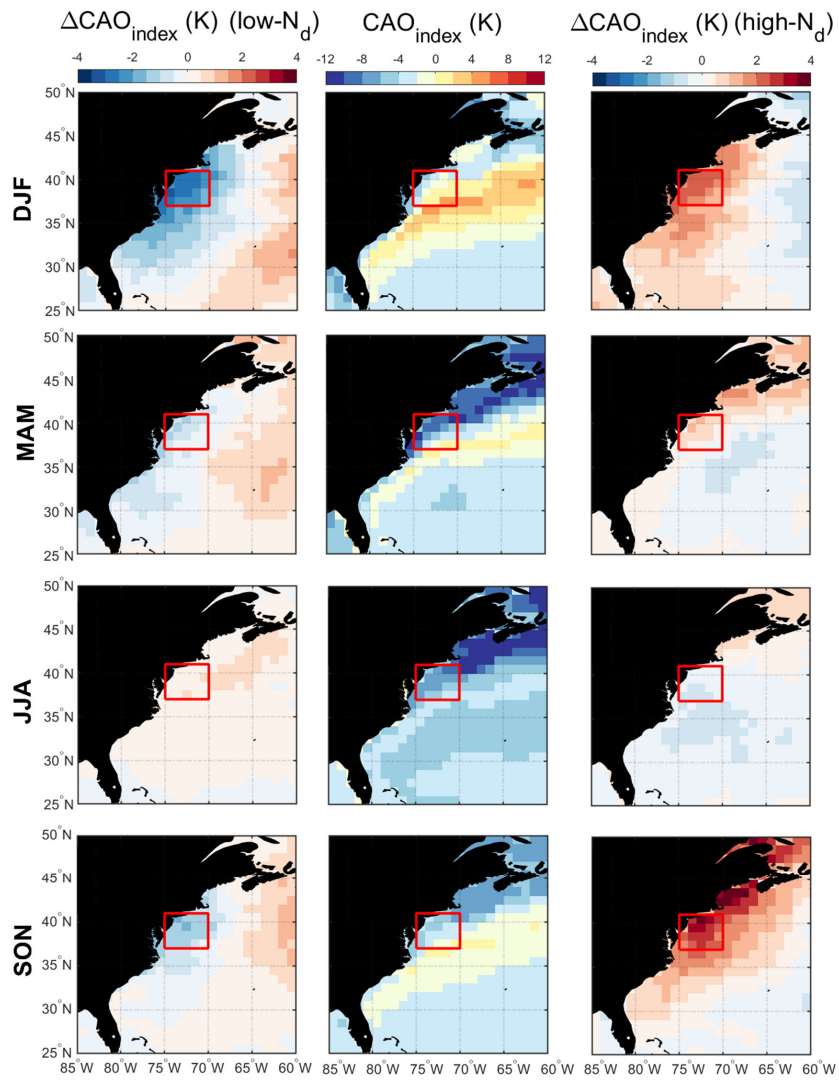


Figure 911: Seasonal averages of cold-air outbreak (CAO) index (middle column) and associated anomalies on low- N_d days (left column) and high- N_d days (right column). The red box represents sub-domain C-N for which the analysis was conducted.

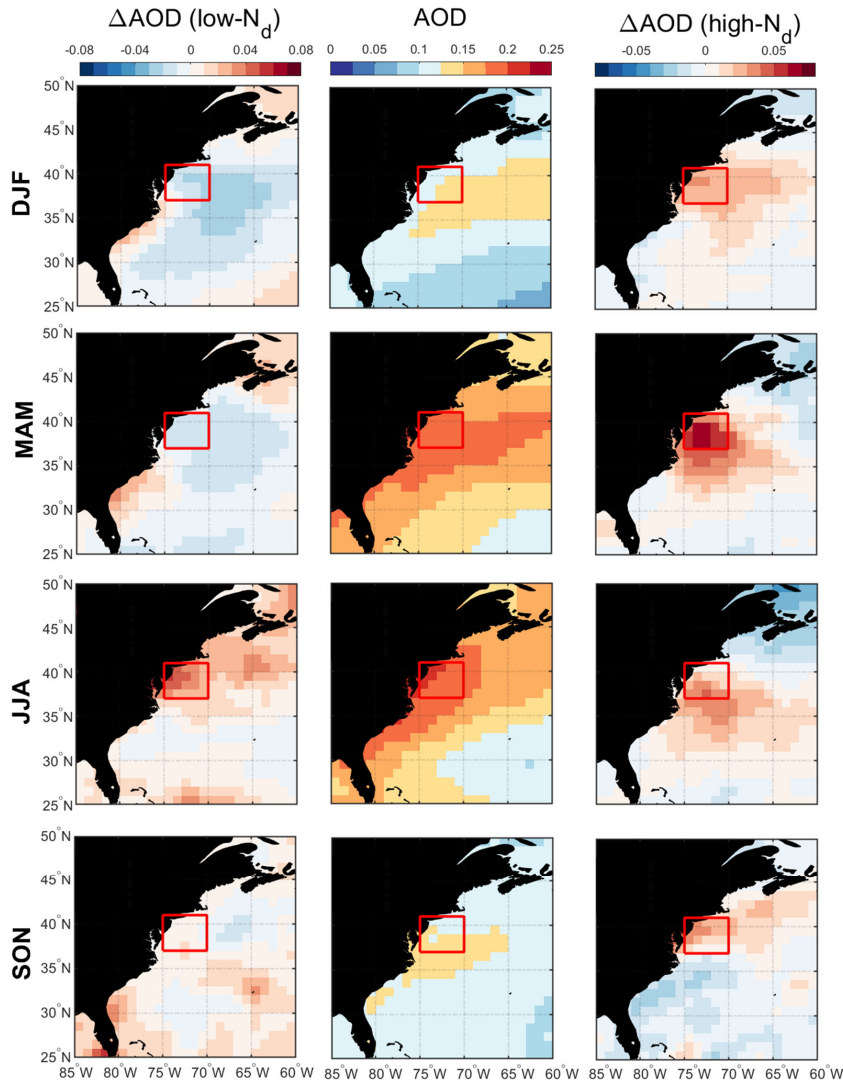


Figure 1012: Seasonal averages of MERRA-2 AOD (middle column) and associated anomalies on low- N_d days (left column) and high- N_d days (right column). The red box represents sub-domain C-N for which the analysis was conducted.

4.2 Multivariate Regression Analysis

Modeling analysis focuses on the two seasons (DJF and JJA) with the extremes in terms of seasonal mean values for N_d and aerosol parameters. Added motivation for examining those two seasons stems from spatial maps of R^2 based on ACI analysis (Figure S23). Using the surface sulfate concentration as the aerosol proxy generally yielded higher R^2 values in three seasons (DJF = 0.13, MAM = 0.05, SON = 0.08) except JJA (0.02) for which the choice did not matter owing to low R^2 (≤ 0.03) values for all four aerosol proxy variables tested. Although the R^2 values are all generally low, DJF and JJA are the seasons when surface sulfate levels are the most and least capable in explaining N_d , with R^2 among the four proxy variables exhibiting the widest (DJF values: 0.07 – 0.13) and narrowest range (JJA: 0.01 – 0.03) of values. We address here how much improvement is gained in modeling N_d by advancing from linear regressions based on one input variable to (i) adding more input variables, and (ii) moving to a more sophisticated model (GBRT) that captures non-linear relationships.

We show in Table 5 the performance of two linear models based on a single linear regression (with sulfate mass concentration), and a multi-regression that uses 14 input variables listed in Table 2. In addition, Table 5 also lists the performance of the GBRT model that ingests 14 inputs variables, similar to the linear multi-regression model. The average R^2 scores of the test set for predicting N_d based on a linear regression using only sulfate surface mass concentration were 0.17 and 0.09 in DJF and JJA, respectively. In contrast, R^2 between the multi-regression linear model and the test dataset increased to 0.28 and 0.26 for DJF and JJA, respectively. This increase in predictive capability was helpful to reduce the gap between seasons by presumably accounting for factors more important in JJA aside from surface concentration of sulfate. The R^2 scores increased even more to 0.457 and 0.439 for DJF and JJA, respectively, for the GBRT model. Therefore, accounting for non-linear relationships improved predictive capability in both seasons. It is important to note that the GBRT model was robust in terms of overfitting and especially generalizability as R^2 values of the test and validation sets were similar for both seasons.

Table 5: Performance of different models in predicting N_d assessed based on average R^2 -scores on both validation and test sets. The models were fitted separately for DJF and JJA seasons. Table 2 has the complete list of variables used in the GBRT model.

Model	Model type	Number of predictor variables	R^2 -score (DJF/JJA)	
			Validation set	Test set
$N_d \sim f(\text{Sulfate}_{\text{sf-mass}})$	Linear	1	0.17/0.10	0.17/0.09
$N_d \sim f(\text{Sulfate}_{\text{sf-mass}}, \text{CF}_{\text{low-liq}}, \dots)$	Linear	12	0.28/0.27	0.28/0.26
$N_d \sim f(\text{Sulfate}_{\text{sf-mass}}, \text{CF}_{\text{low-liq}}, \dots)$	GBRT	12	0.45/0.42	0.45/0.39

Model	Model type	Number of predictor variables	R^2 -score (DJF/JJA)	
			Validation set	Test set
$N_d \sim f(\text{Sulfate}_{\text{sf-mass}})$	Linear	1	0.17/0.09	0.17/0.09
$N_d \sim f(\text{Sulfate}_{\text{sf-mass}}, \text{CF}_{\text{low-liq}}, \dots)$	Linear	14	0.27/0.24	0.28/0.25
$N_d \sim f(\text{Sulfate}_{\text{sf-mass}}, \text{CF}_{\text{low-liq}}, \dots)$	GBRT	14	0.48/0.43	0.47/0.43

We next discuss the importance ranking of different parameters from Table 2 in terms of influencing N_d for DJF and JJA (Figure 413). Low-level liquid cloud fraction was the most

important parameter in both seasons with some commonality in the next three parameters being in common but in different order per for both seasons. In DJF, sulfate surface mass concentrations were the second most important factor, followed by organic carbon surface concentrations and ~~the CAO index~~ low-level liquid cloud-top effective height. As sulfate is secondarily produced via gas-to-particle conversion processes, this result is consistent with those from Figure 1 showing the presumed strong impact of particles smaller than 100 nm in impacting Na values close to shore. In JJA, ~~the CAO index~~ the CAO index was the second most important, followed by organic carbon ~~organic carbon~~ and sulfate surface concentrations. Also, our results throughout the study and supported by modeling are in agreement with Quinn et al. (2017) that sulfate particles contribute more to the CCN budget than sea salt particles. In DJF and JJA, the fifth most important factor ~~was low-level liquid cloud-top effective height~~ was CAO index (~~40th~~ 2nd most important in JJA) and PBLH (~~11th~~ most important in DJF), respectively.

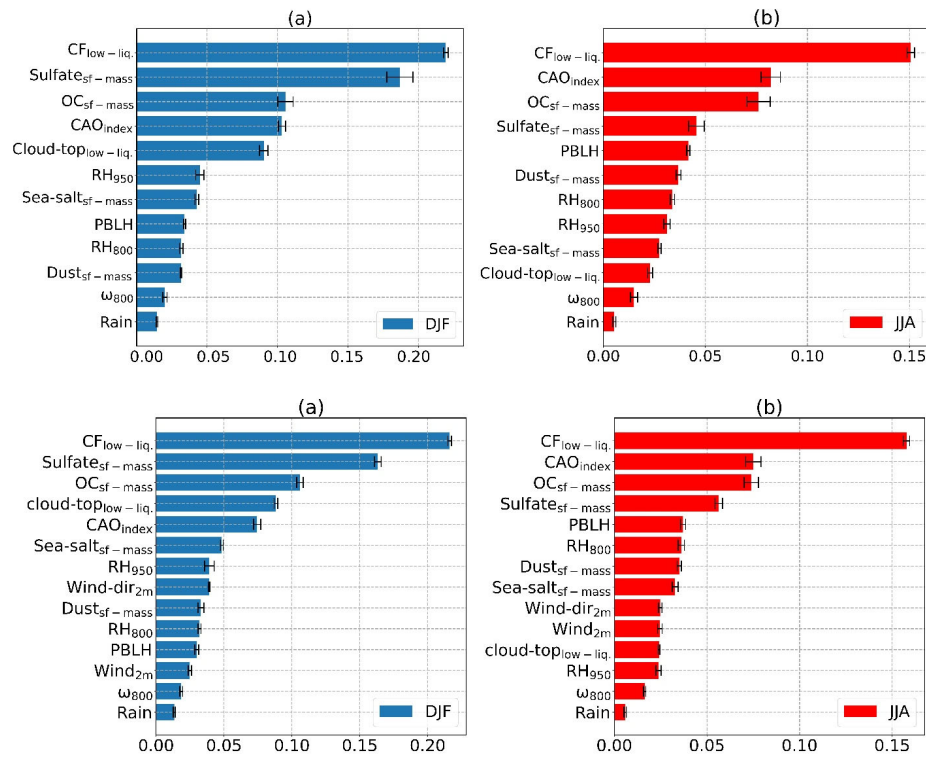


Figure 113: Average permutation feature importance of input parameters for (a) DJF and (b) JJA based on GBRT models trained in each season. Feature importance values were calculated based on using the test set. Error bars exhibit the range of feature importance

values stemming from the variability of the obtained models from the cross-validation resampling procedure.

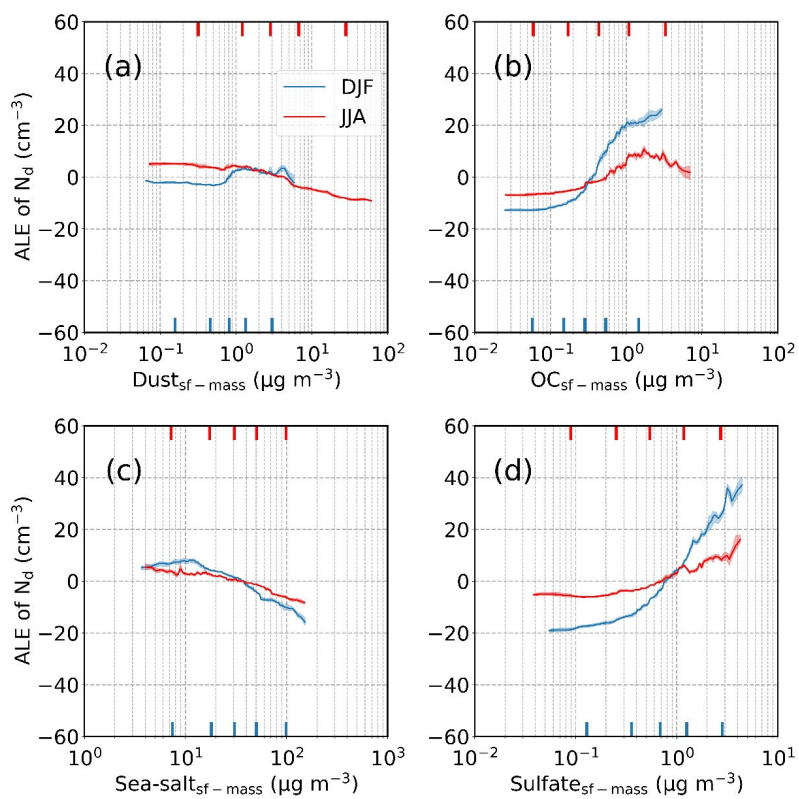
Figures 12-14 and 13-15 show accumulated local effect (ALE) plots for the various parameters ranked in Figure 4-13. In both seasons, but especially DJF, enhanced surface concentrations of sulfate and organic carbon coincide with higher N_d , whereas there was not any obvious positive association between N_d and either sea salt or dust (Figure 12-14). Dust in JJA and sea salt in DJF, seasons of which each respective aerosol type is most predominant, exhibited negative relationships with N_d . Such a negative relationship is plausibly related to differences between ACI when calculated using AOD versus AI (Painemal et al., 2021); for instance, coarse sea salt can expedite collision-coalescence and thus reduce N_d , which has the effect of reducing ACI (Eq. 3) and even possibly yielding negative values (Table 4). Negative values of other ACI constructs coincident with poor R^2 values have previously been attributed to potential effects of giant CCN (Teraï et al., 2015; Dadashazar et al., 2017), but further research needs to examine this in more detail.

Figure 13-15 shows the similarity in the positive relationship between cloud fraction and N_d in both seasons. Only in DJF did cloud-top effective height exhibit a clear relationship with N_d (positive), likely linked to the common phenomenon of CAOs noted in Section 4.1 based on heightened CAO index values, deepening of the boundary layer, and weakened inversion strength. This is supported by enhanced N_d values coincident with negative values for ω_{800} (i.e., rising motion) and CAO index values above 0 in DJF without such relationships in JJA (Figure 13-15). The four-six parameters in Figure S2-12 (PBLH, RH₉₅₀, RH₈₀₀, Rain, Wind_{2m}, Wind-dir_{2m}) did not reveal very pronounced trends with N_d in either season consistent with how they did not rank highly in importance (Figure 4-13). Of particular interest is Wind_{2m}, which is supposed to be used here as a proxy variable represent for the level of turbulence and updraft speed in the marine boundary layer, which was expected to have a high impact on the N_d level via its effect on in-cloud supersaturation. Although the ALE plot of Wind_{2m} suggested a small increase of about $\sim 10 \text{ cm}^{-3}$ in N_d as the wind speed increased, Wind_{2m} did not come out as a very important parameter in either seasons. This may be due to the fact that environmental conditions representing updraft speed were already included in parameters such as cloud fraction and CAO index. Another explanation can be the shortcomings and high uncertainties associated with the use of Wind_{2m} as a proxy for updraft speed.

Formatted: Subscript

Formatted: Superscript

Formatted: Subscript



Formatted: Left

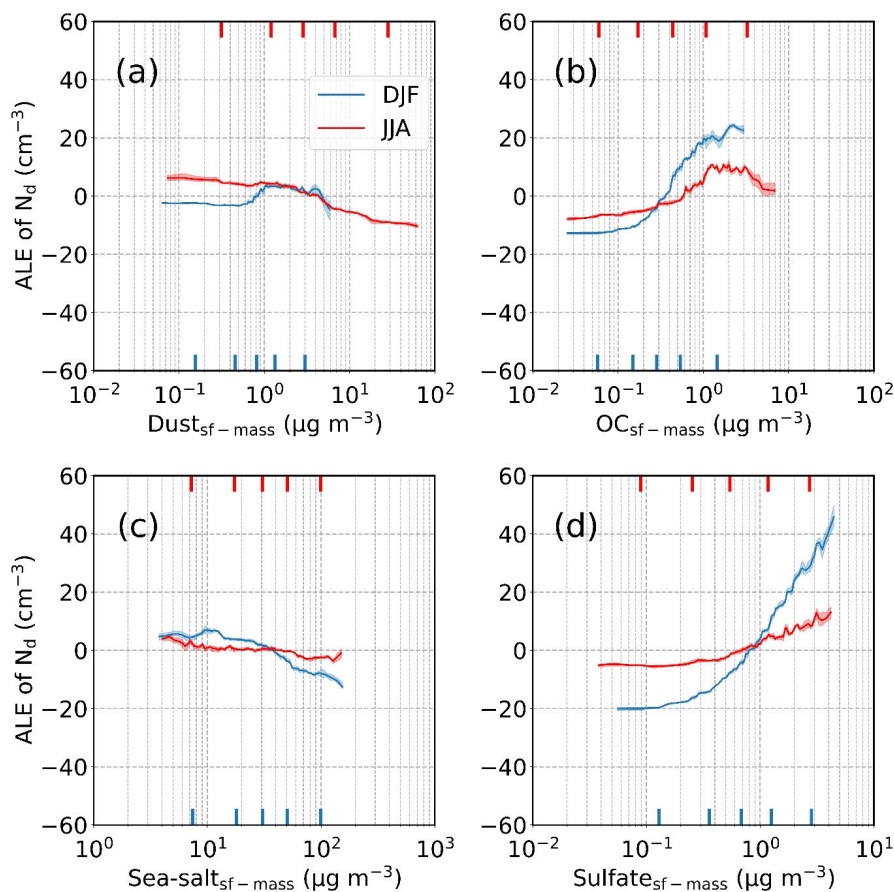
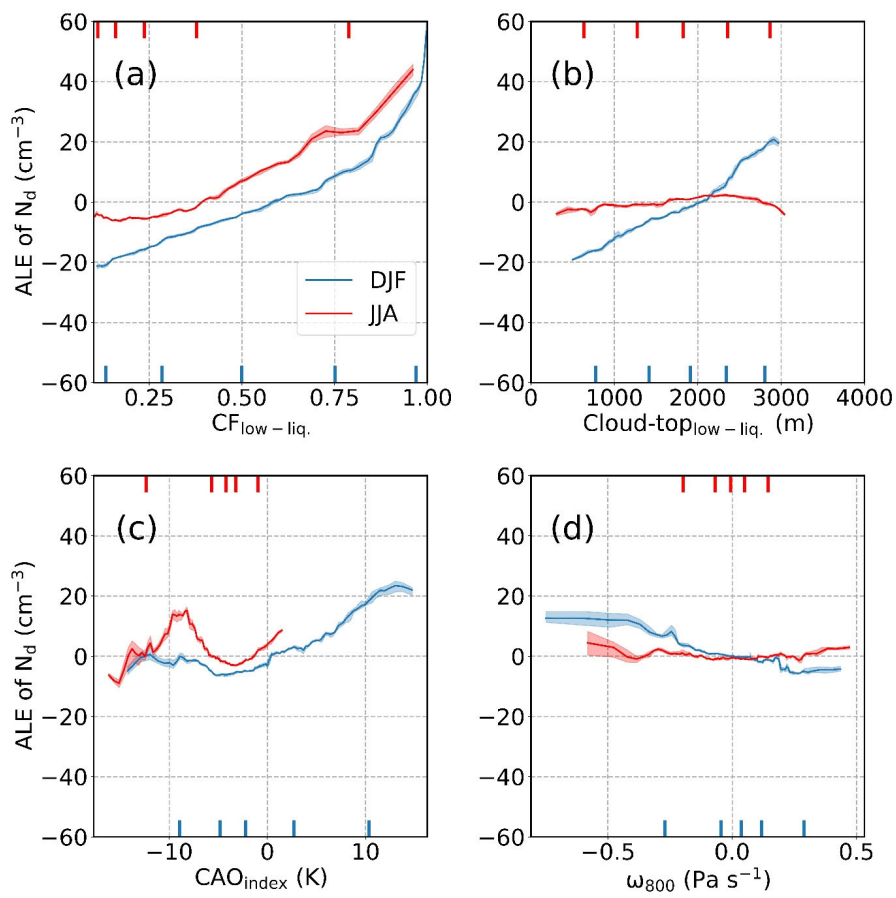


Figure 12.14: Average local accumulated effect (ALE) profiles based on GBRT modeling for surface mass concentrations of the following parameters: (a) dust, (b) organic carbon, (c) sea-salt, and (d) sulfate. Blue and red profiles represent ALEs of DJF and JJA, respectively. Shaded areas show the ALE ranges stemming from the variability of the obtained models from the cross-validation resampling procedure. Markers on the bottom and top x-axes denote the values of 5th, 25th, 50th, 75th, and 95th percentiles for each input variable.

Formatted: Left



Formatted: Centered

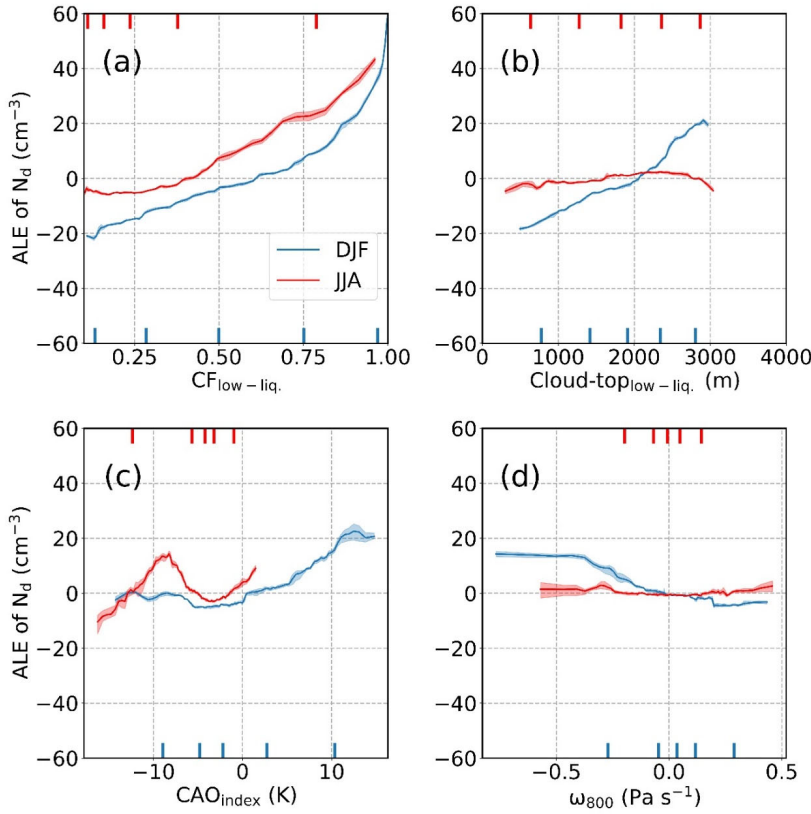


Figure 13.15: Same as Figure 12.14 but for the following input parameters: (a) low-level liquid cloud fraction ($\text{CF}_{\text{low-liq.}}$), (b) cloud-top effective height of low-level liquid cloud ($\text{cloud-top}_{\text{low-liq.}}$), (c) cold-air outbreak (CAO) index, and (d) vertical pressure velocity at 800 hPa (ω_{800}).

The results of regression analysis highlighted the great high sensitivity of N_d to cloud fraction regardless of seasons. As it was discussed earlier, this can be attributed largely to two factors: (i), firstly, the dependency of relationship between cloud regime type (e.g., like stratocumulus, shallow and cumulus) clouds to cloud fraction, which can, in turn, influence cloud microphysical properties like N_d ; and (ii), and secondly, the uncertainties associated with the retrieval of N_d estimates from satellite observations that can results in negative biases in N_d for low cloud coverage conditions. To further test the relative influence of various variables at different cloud fractions, two sensitivity tests with GBRT modeling were conducted using subsets of data where with varying cloud fraction (s were kept either between 0.2 and 0.4 (i.e., $0.2 \leq \text{CF}_{\text{low-}}$

Formatted: Font: Not Bold, Complex Script Font: Not Bold

Formatted: Font: Not Bold, Complex Script Font: Not Bold

Formatted: Indent: First line: 0.5"

Formatted: Font: Not Bold, Complex Script Font: Not Bold

Formatted: Font: Not Bold, Complex Script Font: Not Bold, Subscript

Formatted: Font: Not Bold, Complex Script Font: Not Bold

Formatted: Font: Not Bold, Complex Script Font: Not Bold

Formatted: Font: Not Bold, Complex Script Font: Not Bold

Formatted: Font: Not Bold, Complex Script Font: Not Bold

Formatted: Font: Not Bold, Complex Script Font: Not Bold

Formatted: Font: Not Bold, Complex Script Font: Not Bold

Formatted: Font: Not Bold, Complex Script Font: Not Bold

Formatted: Font: Not Bold, Complex Script Font: Not Bold

Formatted: Font: Not Bold, Complex Script Font: Not Bold

Formatted: Subscript

Formatted: Font: Not Bold, Complex Script Font: Not Bold

Formatted: Font: Not Bold, Complex Script Font: Not Bold

Formatted: Font: Not Bold, Complex Script Font: Not Bold

Formatted: Font: Not Bold, Complex Script Font: Not Bold, Subscript

Formatted: Font: Not Bold, Complex Script Font: Not Bold

Formatted ... [1]

Formatted ... [2]

Formatted: Subscript

Formatted ... [3]

Formatted ... [4]

833 $_{\text{liq.}} < 0.4$ and) or greater than or equal to 0.7 (i.e., $\text{CF}_{\text{low-liq.}} \geq 0.7$). The GBRT models were run on
834 these two subsets of data and the results were presented in SI.

835 Beginning with Figures S24-27 exhibits the results for the subset of data where only
836 samples with $\text{CF}_{\text{low-liq.}} \geq 0.7$ (Figures S242-275), were included in the GBRT models. The average
837 R^2 -scores for validation and test sets for these runs were 0.47/0.39 (DJF/JJA) and 0.49/0.38
838 (DJF/JJA), respectively. A feature that stands out is that for both DJF and JJA, surface mass
839 concentrations of sulfate became the most important factor. ALE plots presented in Fig. S23 also
840 suggested that N_d has a very similar sensitivity to sulfate concentration in high cloud coverage
841 conditions regardless of season in contrast to the results of the original run where N_d was more
842 sensitive to the changes in sulfate level in DJF than JJA. These results are in agreement with
843 various previous studies where N_d values for marine boundary layer clouds were found to be highly
844 sensitive to sulfate concentrations at the level close to cloud base (Boucher and Lohmann, 1995;
845 Lowenthal et al., 2004; Storelvmo et al., 2009; McCoy et al., 2017; McCoy et al., 2018;
846 MacDonald et al., 2020). The second most important factor for DJF was the surface mass
847 concentrations of organic carbon followed by $\text{CF}_{\text{low-liq.}}$, low-level liquid fraction and sea-salt surface
848 mass concentrations. On the other hand, the second most important factor in JJA was CAO index
849 followed by $\text{CF}_{\text{low-liq.}}$ and wind direction. ALE plots presented in Figs. S23-25 showed more or
850 less similar relationships between N_d and input parameters as observed for the original runs where
851 full datasets were used as the input.

852 Figure S26 shows the results of the GBRT model using input data with cloud fraction between
853 0.2 and 0.4, the condition relatively more prevalent in JJA than DJF. The average R^2 -scores for
854 validation and test sets for these runs were 0.30/0.30 (DJF/JJA) and 0.33/0.31 (DJF/JJA),
855 respectively. It is interesting to see that for both seasons, an aerosol parameter turned out merged
856 as the most important factor, however, ~~mass~~ concentrations of OC appeared as the most
857 important factor in JJA (the fourth most important factor in DJF) while in DJF, sulfate
858 concentration came out as the most important factor (the fourth most important factor in JJA)
859 consistent with the results of previously discussed models for DJF. It should be noted that ALE
860 plots also suggested less sensitivity of N_d to sulfate level in JJA than DJF, similar to the results
861 observed in the original model run including all the data points. The second most important factor
862 in DJF turned out to be the cloud-top effective height of low-level liquid clouds followed by CAO
863 index. On the other hand, CAO index was the second most important factor in JJA followed by
864 PBLH. ALE plots presented in Figs. S27-29 also showed similar qualitative trends observed in
865 original and high cloud coverage runs.

867 4.3 Unexplored Factors

868 Additional factors impacting the relationship between aerosol and N_d seasonal cycles are
869 discussed here that warrant additional research with more detailed data at finer scales such as with
870 aircraft. We are cognizant that this list is not fully exhaustive. As low-level cloud fraction impacted
871 model results of Section 4.2 so substantially, the dynamics of the studied clouds require further
872 characterization. As cloud fraction and CAO index are well related, especially in DJF, aerosol-
873 cloud interactions likely are stronger than other seasons (as implied by Section 3.5) due in part to

Formatted: Font: Not Bold, Complex Script Font: Not Bold, Not Superscript/ Subscript

Formatted: Font: Not Bold, Complex Script Font: Not Bold

Formatted: Font: Not Bold, Complex Script Font: Not Bold

Formatted: Font: Not Bold, Complex Script Font: Not Bold, Not Superscript/ Subscript

Formatted: Font: Not Bold, Complex Script Font: Not Bold

Formatted: Font: Not Bold, Complex Script Font: Not Bold

Formatted: Superscript

Formatted: Subscript

Formatted: Subscript

Formatted: Subscript

Formatted: Subscript

Formatted: Indent: First line: 0.25"

Formatted: Subscript

Formatted: Font: Not Bold, Complex Script Font: Not Bold

Formatted: Font: Not Bold, Complex Script Font: Not Bold

enhanced surface fluxes and turbulence, and thus more droplet activation with higher cloud supersaturations (Painemal et al., 2021); in contrast, the smaller shallow cumulus clouds in summertime may be less favorable for droplet activation due to factors such as reduced turbulence and more lateral entrainment.

Entrainment of free tropospheric aerosol can impact N_d values, with potentially varying degrees of influence between seasons. It is presumed that with summertime convection, the more broken cumulus scenes are less adiabatic through the cloudy column and more affected by entrainment and mixing; hence, N_d values derived using data that remote sensors retrieve near cloud top could be considerably lower than values lower by cloud base. Satellite remote sensing studies of aerosol-cloud interactions ~~will struggle for~~ presumably will be more challenging in analyzing winter periods versus the summer with regard to data as compared to summertime because of the varying degree of the spatial and temporal mismatch ~~in different seasons~~ between cloud and aerosol retrievals. More specifically, it is easier to get nearly coincidental sampling in summertime due to lower cloud fractions, while in winter the frontal regions with high cloud fractions make it challenging to get aerosol retrievals. There is complexity in understanding how aerosols relate to N_d due to how giant CCN can reduce N_d and also since wet scavenging can remove aerosols efficiently. As aircraft data are limited and difficult to use for assessing seasonal cycles, new techniques of retrieving CCN and N_d from space will greatly assist such types of studies in the future.

5. Conclusions

This work investigates the seasonal cycle of N_d over the WNAO region in terms of concentration statistics and with discussion of potential influential factors. The results of this work have implications for increased understanding of aerosol-cloud interactions and meteorological factors influencing concentration of cloud droplets in the marine boundary layer. The results and interpretations can be summarized as follows in the order of how they were presented:

- An ACTIVATE case flight during the DJF season shows a sharp offshore N_d gradient ranging from $> 1000 \text{ cm}^{-3}$ to $< 50 \text{ cm}^{-3}$ explained in part by particles smaller than 100 nm activating into drops during a cold air outbreak with post-frontal clouds. There were significant changes in aerosol composition in cloud-free air and also in droplet residual particles as a function of offshore distance. These changes included a sharp decrease in aerosol number concentration, a decrease in mass fraction of sulfate in droplet residual particles, and an increase in mass fraction of organic and chloride of droplet residual particles moving offshore.
- N_d is generally highest (lowest) in DJF (JJA) over the WNAO but aerosol parameters such as AOD, AI, ~~and~~ surface-based aerosol mass concentrations for most species, and CCN concentrations (1% supersaturation) are generally highest in JJA and MAM and are at (or near) their lowest values in DJF. While aerosol extinction in the PBL is highest in DJF, it is driven largely by sea salt (large but few in number), and thus cannot explain the N_d peak in wintertime.
- While relative humidity was generally highest in JJA across the WNAO, the differences between seasons in the PBL and FT were not sufficiently large to explain the divergent seasonal cycles of AOD and N_d .

- The susceptibility of N_d to aerosols (Eq. 3) was strongest in DJF using four different proxy variables for aerosols, suggestive of at least one reason why N_d can be highest when aerosol proxy variables for concentration are typically near or at their lowest values.
- Composite maps of high versus low N_d days across the WNAO reveal that conditions associated with the highest N_d days, regardless of season (but especially DJF) are reduced sea level pressure, stronger winds aligned with continental outflow, high low-level liquid cloud fraction, higher CAO index and PBLH, and enhanced AOD. Cold air outbreaks are coincident with all of these conditions, especially in the colder months of DJF in sharp contrast to JJA when N_d is lowest.
- Gradient boosted regression analysis shows that the most important predictors of N_d in DJF and JJA vary to some extent, but with cloud fraction being the most important parameter, followed by either (for DJF) surface mass concentrations of sulfate and organic carbon and CAO index or (for JJA) CAO index, surface mass concentrations of organic carbon, and sulfate concentrations. Accumulated local effect plots confirm that sulfate and organics help drive the high N_d values via continental outflow, which is assisted in large part by conditions associated with CAOs~~by CAO type of conditions~~ such as high cloud fraction and high CAO index.

Therefore, the combination of continental pollution outflow and turbulence changes contributed by surface fluxes (manifested in strongest CAO index values in DJF and weakest in JJA) markedly influence the N_d cycle, leading to differing annual cycles in cloud microphysics and aerosols. More detailed data such as from aircraft and modeling can help extend this line of research to confirm these findings and speculations such as how (i) the aerosol indirect effect is strongest in DJF due to boundary layer dynamics such as with more turbulence and mixing than other seasons (Painemal et al., 2021); (ii) enhanced giant CCN in forms such as sea salt and dust can reduce N_d via expediting the collision-coalescence process; and (iii) substantial aerosol removal can occur far offshore as postfrontal clouds associated with CAOs build and then begin to precipitate. The latter hypothesis may help explain why Bermuda (> 1000 km offshore the U.S. East Coast) was the only selected sub-domain in this study to not have a seasonal N_d peak in DJF.

948 *Data Availability.*

949 CERES-MODIS: <https://ceres.larc.nasa.gov/data/>

950 CALIPSO: <https://subset.larc.nasa.gov/calipso>

951 PERSIANN-CDR: <https://chrsdata.eng.uci.edu/>

952 MERRA-2: <https://disc.gsfc.nasa.gov/>

953 TCAP CCN: <https://adc.arm.gov/discovery>

954 ACTIVATE Airborne Data: <https://www-air.larc.nasa.gov/cgi-bin/ArcView/activate.2019>

955 *Author contributions.* HD, DP, and MA conducted the analysis. AS and HD prepared the

956 manuscript. All authors contributed by providing input and/or participating in airborne data

957 collection.

958 *Competing interests.* The authors declare that they have no conflict of interest.

959 *Acknowledgments.* The work was funded by NASA grant 80NSSC19K0442 in support of

960 ACTIVATE, a NASA Earth Venture Suborbital-3 (EVS-3) investigation funded by NASA's

961 Earth Science Division and managed through the Earth System Science Pathfinder Program

962 Office. The authors acknowledge the NOAA Air Resources Laboratory (ARL) for the provision

963 of the HYSPLIT transport and dispersion model and READY website (<http://ready.arl.noaa.gov>)

964 used in this work.

965 **References**

966 Abel, S. J., Boutle, I. A., Waite, K., Fox, S., Brown, P. R. A., Cotton, R., Lloyd, G., Choulaton,

967 T. W., and Bower, K. N.: The Role of Precipitation in Controlling the Transition from

968 Stratocumulus to Cumulus Clouds in a Northern Hemisphere Cold-Air Outbreak, *J Atmos Sci*,

969 74, 2293-2314, 10.1175/Jas-D-16-0362.1, 2017.

970 Ackerman, A.S., Kirkpatrick, M.P., Stevens, D.E., Toon, O.B.: The impact of humidity above

971 stratiform clouds on indirect aerosol climate forcing, *Nature* 432, 1014–1017,

972 doi:10.1038/nature03174, 2004.

973 Albrecht, B. A.: Aerosols, Cloud Microphysics, and Fractional Cloudiness, *Science*, 245, 1227-

974 1230, 10.1126/science.245.4923.1227, 1989.

975 ~~Aldhaif, A.M., Lopez, D.H., Dadashazar, H., Painemal, D., Peters, A.J., Sorooshian, A.: An~~

976 ~~Aerosol Climatology and Implications for Clouds at a Remote Marine Site: Case Study Over~~

977 ~~Bermuda, *Journal of Geophysical Research: Atmospheres* 126, doi:10.1029/2020jd034038,~~

978 ~~2021.~~

979 ~~Aldhaif, A. M., Lopez, D. H., Dadashazar, H., Painemal, D., Peters, A. J., Sorooshian, A.: An~~

980 ~~Aerosol Climatology and Implications for Clouds at a Remote Marine Site: Case Study over~~

981 ~~Bermuda, *J Geophys Res Atmos*, accepted, 2021.~~

982 Apley, D. W., and Zhu, J. Y.: Visualizing the effects of predictor variables in black box

983 supervised learning models, *J R Stat Soc B*, 82, 1059-1086, 10.1111/rssb.12377, 2020.

984 Ashouri, H., Hsu, K.-L., Sorooshian, S., Braithwaite, D. K., Knapp, K. R., Cecil, L. D., Nelson,

985 B. R. and Prat, O. P.: PERSIANN-CDR: Daily Precipitation Climate Data Record from

Formatted: EndNote Bibliography, Left, Adjust space between Latin and Asian text, Adjust space between Asian text and numbers

Formatted: Font: Not Bold, Font color: Auto, Complex Script Font: Not Bold

Formatted: EndNote Bibliography

Formatted: EndNote Bibliography

986 Multisatellite Observations for Hydrological and Climate Studies, *Bull. Am. Meteorol. Soc.*,
 987 96(1), 69–83, <https://doi.org/10.1175/BAMS-D-13-00068.1>, 2015.
 988 Bennartz, R., Fan, J. W., Rausch, J., Leung, L. R., and Heidinger, A. K.: Pollution from China
 989 increases cloud droplet number, suppresses rain over the East China Sea, *Geophys Res Lett*, 38,
 990 10.1029/2011gl047235, 2011.
 991 Berg, L. K., Fast, J. D., Barnard, J. C., Burton, S. P., Cairns, B., Chand, D., Comstock, J. M.,
 992 Dunagan, S., Ferrare, R. A., Flynn, C. J., Hair, J. W., Hostetler, C. A., Hubbe, J., Jefferson, A.,
 993 Johnson, R., Kassianov, E. I., Kluzek, C. D., Kollias, P., Lamer, K., Lantz, K., Mei, F., Miller,
 994 M. A., Michalsky, J., Ortega, I., Pekour, M., Rogers, R. R., Russell, P. B., Redemann, J.,
 995 Sedlacek, A. J., Segal-Rosenheimer, M., Schmid, B., Shilling, J. E., Shinozuka, Y., Springston,
 996 S. R., Tomlinson, J. M., Tyrrell, M., Wilson, J. M., Volkamer, R., Zelenyuk, A., and Berkowitz,
 997 C. M.: The Two-Column Aerosol Project: Phase I Overview and impact of elevated aerosol
 998 layers on aerosol optical depth, *J Geophys Res-Atmos*, 121, 336–361, 10.1002/2015jd023848,
 999 2016.
 1000 Berg, W., L'Ecuyer, T., and van den Heever, S.: Evidence for the impact of aerosols on the onset
 1001 and microphysical properties of rainfall from a combination of satellite observations and cloud-
 1002 resolving model simulations, *J Geophys Res-Atmos*, 113, 10.1029/2007jd009649, 2008.
 1003 Boucher, O., and Lohmann, U.: The Sulfate-Ccn-Cloud Albedo Effect - a Sensitivity Study with
 1004 2 General-Circulation Models, *Tellus B*, 47, 281–300, 10.1034/j.1600-0889.47.issue3.1.x, 1995.
 1005 Boucher, O., Randall, D., Artaxo, P., Bretherton, C., Feingold, G., Forster, P., Kerminen, V.-M.,
 1006 Kondo, Y., Liao, H., Lohmann, U., Rasch, P., Satheesh, S. K., Sherwood, S., Stevens, B., and
 1007 Zhang, X. Y.: Clouds and aerosols, in: *Climate Change 2013: The Physical Science Basis. Contribution of Working Group I to the Fifth Assessment Report of the Intergovernmental Panel on Climate Change*, edited by: Stocker, T. F., Qin, D., Plattner, G.-K., Tignor, M., Allen, S. K.,
 1008 Doschung, J., Nauels, A., Xia, Y., Bex, V., and Midgley, P. M., Cambridge University Press,
 1009 Cambridge, UK, 571–657, 2013.
 1010 Breon, F. M., Tanre, D., and Generoso, S.: Aerosol effect on cloud droplet size monitored from
 1011 satellite, *Science*, 295, 834–838, 10.1126/science.1066434, 2002.
 1012 Brummer, B.: Boundary-layer modification in wintertime cold-air outbreaks from the arctic sea
 1013 ice, *Bound-Lay Meteorol*, 80, 109–125, 10.1007/Bf00119014, 1996.
 1014 Buchard, V., Randles, C. A., da Silva, A. M., Darmenov, A., Colarco, P. R., Govindaraju, R.,
 1015 Ferrare, R., Hair, J., Beyersdorf, A. J., Ziemba, L. D., and Yu, H.: The MERRA-2 Aerosol
 1016 Reanalysis, 1980 Onward. Part II: Evaluation and Case Studies, *J Climate*, 30, 6851–6872,
 1017 10.1175/Jcli-D-16-0613.1, 2017.
 1018 Chin, M., Ginoux, P., Kinne, S., Torres, O., Holben, B. N., Duncan, B. N., Martin, R. V., Logan,
 1019 J. A., Higurashi, A., and Nakajima, T.: Tropospheric Aerosol Optical Thickness from the
 1020 GOCART Model and Comparisons with Satellite and Sun Photometer Measurements, *Journal of*
 1021 *the Atmospheric Sciences*, 59, 461–483, 10.1175/1520-
 1022 0469(2002)059<0461:TAOTFT>2.0.CO;2, 2002.
 1023 Colarco, P., da Silva, A., Chin, M., and Diehl, T.: Online simulations of global aerosol
 1024 distributions in the NASA GEOS-4 model and comparisons to satellite and ground-based aerosol
 1025 optical depth, *Journal of Geophysical Research: Atmospheres*, 115,
 1026 <https://doi.org/10.1029/2009JD012820>, 2010.
 1027 Corral, A. F., Braun, R., Cairns, B., Gorooh, V. A., Liu, H., Ma, L., Mardi, A., Painemal, D.,
 1028 Stamnes, S., van Diedenhoven, B., Wang, H., Yang, Y., Zhang, B., and Sorooshian, A.: An
 1029 Overview of Atmospheric Features Over the Western North Atlantic Ocean and North American
 1030
 1031

1032 East Coast – Part 1: Analysis of Aerosols, Gases, and Wet Deposition Chemistry J Geophys Res-
 1033 Atmos, 10.1029/2020JD032592, 2021.
 1034 Dadashazar, H., Wang, Z., Crosbie, E., Brunke, M., Zeng, X. B., Jonsson, H., Woods, R. K.,
 1035 Flagan, R. C., Seinfeld, J. H., and Sorooshian, A.: Relationships between giant sea salt particles
 1036 and clouds inferred from aircraft physicochemical data, J Geophys Res-Atmos, 122, 3421-3434,
 1037 10.1002/2016jd026019, 2017.
 1038 Dadashazar, H., Crosbie, E., Majdi, M. S., Panahi, M., Moghaddam, M. A., Behrangi, A.,
 1039 Brunke, M., Zeng, X. B., Jonsson, H. H., and Sorooshian, A.: Stratocumulus cloud clearings:
 1040 statistics from satellites, reanalysis models, and airborne measurements, Atmos Chem Phys, 20,
 1041 4637-4665, 10.5194/acp-20-4637-2020, 2020.
 1042 DeCarlo, P. F., Dunlea, E. J., Kimmel, J. R., Aiken, A. C., Sueper, D., Crounse, J., Wennberg, P.
 1043 O., Emmons, L., Shinozuka, Y., Clarke, A., Zhou, J., Tomlinson, J., Collins, D. R., Knapp, D.,
 1044 Weinheimer, A. J., Montzka, D. D., Campos, T., and Jimenez, J. L.: Fast airborne aerosol size
 1045 and chemistry measurements above Mexico City and Central Mexico during the MILAGRO
 1046 campaign, Atmos Chem Phys, 8, 4027-4048, 10.5194/acp-8-4027-2008, 2008.
 1047 Deuze, J. L., Breon, F. M., Devaux, C., Goloub, P., Herman, M., Lafrance, B., Maignan, F.,
 1048 Marchand, A., Nadal, F., Perry, G., and Tanre, D.: Remote sensing of aerosols over land surfaces
 1049 from POLDER-ADEOS-1 polarized measurements, J Geophys Res-Atmos, 106, 4913-4926,
 1050 10.1029/2000jd900364, 2001.
 1051 [Feingold, G.: Modeling of the first indirect effect: Analysis of measurement requirements.](#)
 1052 [Geophysical Research Letters 30, doi:10.1029/2003gl017967, 2003.](#)
 1053 Fletcher, J., Mason, S., and Jakob, C.: The Climatology, Meteorology, and Boundary Layer
 1054 Structure of Marine Cold Air Outbreaks in Both Hemispheres, J Climate, 29, 1999-2014,
 1055 10.1175/Jcli-D-15-0268.1, 2016.
 1056 Fuchs, J., Cermak, J., and Andersen, H.: Building a cloud in the southeast Atlantic:
 1057 understanding low-cloud controls based on satellite observations with machine learning, Atmos
 1058 Chem Phys, 18, 16537-16552, 10.5194/acp-18-16537-2018, 2018.
 1059 Gelaro, R., McCarty, W., Suarez, M. J., Todling, R., Molod, A., Takacs, L., Randles, C. A.,
 1060 Darmenov, A., Bosilovich, M. G., Reichle, R., Wargan, K., Coy, L., Cullather, R., Draper, C.,
 1061 Akella, S., Buchard, V., Conaty, A., da Silva, A. M., Gu, W., Kim, G. K., Koster, R., Lucchesi,
 1062 R., Merkova, D., Nielsen, J. E., Partyka, G., Pawson, S., Putman, W., Rienecker, M., Schubert,
 1063 S. D., Sienkiewicz, M., and Zhao, B.: The Modern-Era Retrospective Analysis for Research and
 1064 Applications, Version 2 (MERRA-2), J Climate, 30, 5419-5454, 10.1175/Jcli-D-16-0758.1,
 1065 2017.
 1066 Grandey, B. S., and Stier, P.: A critical look at spatial scale choices in satellite-based aerosol
 1067 indirect effect studies, Atmos. Chem. Phys., 10, 11459-11470, 10.5194/acp-10-11459-2010,
 1068 2010.
 1069 Grosvenor, D. P., Sourdeval, O., Zuidema, P., Ackerman, A., Alexandrov, M. D., Bennartz, R.,
 1070 Boers, R., Cairns, B., Chiu, J. C., Christensen, M., Deneke, H., Diamond, M., Feingold, G.,
 1071 Fridlind, A., Hunerbein, A., Knist, C., Kollias, P., Marshak, A., McCoy, D., Merk, D., Painemal,
 1072 D., Rausch, J., Rosenfeld, D., Russchenberg, H., Seifert, P., Sinclair, K., Stier, P., van
 1073 Diedenhoven, B., Wendisch, M., Werner, F., Wood, R., Zhang, Z. B., and Quaas, J.: Remote
 1074 Sensing of Droplet Number Concentration in Warm Clouds: A Review of the Current State of
 1075 Knowledge and Perspectives, Rev Geophys, 56, 409-453, 10.1029/2017rg000593, 2018.
 1076 Gryspeerdt, E., Quaas, J., and Bellouin, N.: Constraining the aerosol influence on cloud fraction,
 1077 J Geophys Res-Atmos, 121, 3566-3583, 10.1002/2015jd023744, 2016.

1078 Gryspeerd, E., Quaas, J., Ferrachat, S., Gettelman, A., Ghan, S., Lohmann, U., Morrison, H.,
 1079 Neubauer, D., Partridge, D. G., Stier, P., Takemura, T., Wang, H. L., Wang, M. H., and Zhang,
 1080 K.: Constraining the instantaneous aerosol influence on cloud albedo, *P Natl Acad Sci USA*, 114,
 1081 4899-4904, 10.1073/pnas.1617765114, 2017.
 1082 Hasekamp, O. P., Gryspeerd, E., and Quaas, J.: Analysis of polarimetric satellite measurements
 1083 suggests stronger cooling due to aerosol-cloud interactions, *Nat Commun*, 10, 10.1038/s41467-
 1084 019-13372-2, 2019.
 1085 Hastie, T., Tibshirani, R., and Friedman, J.: *The elements of statistical learning: data mining,*
 1086 *inference and prediction*, 2 ed., Springer, 2009.
 1087 Kim, M. H., Omar, A. H., Vaughan, M. A., Winker, D. M., Trepte, C. R., Hu, Y. X., Liu, Z. Y.,
 1088 and Kim, S. W.: Quantifying the low bias of CALIPSO's column aerosol optical depth due to
 1089 undetected aerosol layers, *J Geophys Res-Atmos*, 122, 1098-1113, 10.1002/2016jd025797, 2017.
 1090 Kolstad, E. W., Bracegirdle, T. J., and Seierstad, I. A.: Marine cold-air outbreaks in the North
 1091 Atlantic: temporal distribution and associations with large-scale atmospheric circulation, *Clim*
 1092 *Dynam*, 33, 187-197, 10.1007/s00382-008-0431-5, 2009.
 1093 Liu, J. J., and Li, Z. Q.: Aerosol properties and their influences on low warm clouds during the
 1094 Two-Column Aerosol Project, *Atmos Chem Phys*, 19, 9515-9529, 10.5194/acp-19-9515-2019,
 1095 2019.
 1096 Lloyd, G., Choularton, T. W., Bower, K. N., Gallagher, M. W., Crosier, J., O'Shea, S., Abel, S.
 1097 J., Fox, S., Cotton, R., and Boutle, I. A.: In situ measurements of cloud microphysical and
 1098 aerosol properties during the break-up of stratocumulus cloud layers in cold air outbreaks over
 1099 the North Atlantic, *Atmos Chem Phys*, 18, 17191-17206, 10.5194/acp-18-17191-2018, 2018.
 1100 Loeb, N. G., Manalo-Smith, N., Su, W. Y., Shankar, M., and Thomas, S.: CERES Top-of-
 1101 Atmosphere Earth Radiation Budget Climate Data Record: Accounting for in-Orbit Changes in
 1102 Instrument Calibration, *Remote Sens-Basel*, 8, 10.3390/rs8030182, 2016.
 1103 Lowenthal, D. H., Borys, R. D., Choularton, T. W., Bower, K. N., Flynn, M. J., and Gallagher,
 1104 M. W.: Parameterization of the cloud droplet-sulfate relationship, *Atmospheric Environment*, 38,
 1105 287-292, 10.1016/j.atmosenv.2003.09.046, 2004.
 1106 MacDonald, A. B., Mardi, A. H., Dadashazar, H., Aghdam, M. A., Crosbie, E., Jonsson, H. H.,
 1107 Flagan, R. C., Seinfeld, J. H., and Sorooshian, A.: On the relationship between cloud water
 1108 composition and cloud droplet number concentration, *Atmos Chem Phys*, 20, 7645-7665,
 1109 10.5194/acp-20-7645-2020, 2020.
 1110 McComiskey, A., Feingold, G., Frisch, A. S., Turner, D. D., Miller, M. A., Chiu, J. C., Min, Q.
 1111 L., and Ogren, J. A.: An assessment of aerosol-cloud interactions in marine stratus clouds based
 1112 on surface remote sensing, *J Geophys Res-Atmos*, 114, 10.1029/2008jd011006, 2009.
 1113 McCoy, D. T., Bender, F. A. M., Mohrmann, J. K. C., Hartmann, D. L., Wood, R., and
 1114 Grosvenor, D. P.: The global aerosol-cloud first indirect effect estimated using MODIS,
 1115 MERRA, and AeroCom, *J Geophys Res-Atmos*, 122, 1779-1796, 10.1002/2016jd026141, 2017.
 1116 McCoy, D. T., Bender, F. A. M., Grosvenor, D. P., Mohrmann, J. K., Hartmann, D. L., Wood,
 1117 R., and Field, P. R.: Predicting decadal trends in cloud droplet number concentration using
 1118 reanalysis and satellite data, *Atmos Chem Phys*, 18, 2035-2047, 10.5194/acp-18-2035-2018,
 1119 2018.
 1120 Minnis, P., Sun-Mack, S., Young, D. F., Heck, P. W., Garber, D. P., Chen, Y., Spangenberg, D.
 1121 A., Arduini, R. F., Trepte, Q. Z., Smith, W. L., Ayers, J. K., Gibson, S. C., Miller, W. F., Hong,
 1122 G., Chakrapani, V., Takano, Y., Liou, K. N., Xie, Y., and Yang, P.: CERES Edition-2 Cloud

1123 Property Retrievals Using TRMM VIRS and Terra and Aqua MODIS Data-Part I: Algorithms,
 1124 Ieee T Geosci Remote, 49, 4374-4400, 10.1109/Tgrs.2011.2144601, 2011.
 1125 Minnis, P., Sun-Mack, S., Chen, Y., Chang, F., Yost, C. R., Smith, W. L., Heck, P. W., Arduini,
 1126 R. F., Bedka, S. T., Yi, Y., Hong, G., Jin, Z., Painemal, D., Palikonda, R., Scarino, B. R.,
 1127 Spangenberg, D. A., Smith, R. A., Trepte, Q. Z., Yang, P., and Xie, Y.: CERES MODIS Cloud
 1128 Product Retrievals for Edition 4--Part I: Algorithm Changes, Ieee T Geosci Remote, 1-37,
 1129 10.1109/TGRS.2020.3008866, 2020.
 1130 Molnar, C.: Interpretable Machine Learning. A Guide for Making Black Box Models
 1131 Explainable, <https://christophm.github.io/interpretable-ml-book/>, 2019.
 1132 Myhre, G., Shindell, D., Bréon, F.-M., Collins, W., Fuglestad, J., Huang, J., Koch, D.,
 1133 Lamarque, J.-F., Lee, D., Mendoza, B., Nakajima, T., Robock, A., Stephens, G., Takemura, T.,
 1134 and Zhang, H.: Anthropogenic and natural radiative forcing, in: Climate Change 2013: The
 1135 Physical Science Basis. Contribution of Working Group I to the Fifth Assessment Report of the
 1136 Intergovernmental Panel on Climate Change, edited by: Stocker, T. F., Qin, D., Plattner, G.-K.,
 1137 Tignor, M., Allen, S. K., Doschung, J., Nauels, A., Xia, Y., Bex, V., and Midgley, P. M.,
 1138 Cambridge University Press, Cambridge, UK, 659-740, 2013.
 1139 Nakajima, T., Higurashi, A., Kawamoto, K., and Penner, J. E.: A possible correlation between
 1140 satellite-derived cloud and aerosol microphysical parameters, Geophys Res Lett, 28, 1171-1174,
 1141 10.1029/2000gl012186, 2001.
 1142 Naud, C. M., Booth, J. F., and Lamraoui, F.: Post Cold Frontal Clouds at the ARM Eastern North
 1143 Atlantic Site: An Examination of the Relationship Between Large-Scale Environment and Low-
 1144 Level Cloud Properties, J Geophys Res-Atmos, 123, 12117-12132, 10.1029/2018jd029015,
 1145 2018.
 1146 Nguyen, P., Ombadi, M., Sorooshian, S., Hsu, K., AghaKouchak, A., Braithwaite, D., Ashouri,
 1147 H. and Thorstensen, A. R.: The PERSIANN family of global satellite precipitation data: a review
 1148 and evaluation of products, Hydrol. Earth Syst. Sci., 22(11), 5801-5816,
 1149 <https://doi.org/10.5194/hess-22-5801-2018>, 2018.
 1150 Painemal, D.: Global Estimates of Changes in Shortwave Low-Cloud Albedo and Fluxes Due to
 1151 Variations in Cloud Droplet Number Concentration Derived From CERES-MODIS Satellite
 1152 Sensors, Geophys Res Lett, 45, 9288-9296, 10.1029/2018gl078880, 2018.
 1153 Painemal, D., Chang, F. L., Ferrare, R., Burton, S., Li, Z., Smith Jr, W. L., Minnis, P., Feng, Y.,
 1154 and Clayton, M.: Reducing uncertainties in satellite estimates of aerosol-cloud interactions over
 1155 the subtropical ocean by integrating vertically resolved aerosol observations, Atmos Chem Phys,
 1156 20, 7167-7177, 10.5194/acp-20-7167-2020, 2020.
 1157 Painemal, D., Corral, A. F., Sorooshian, A., Brunke, M. A., Chellappan, S., Gorooh, V. A., Ham,
 1158 S., O'Neill, L., Smith Jr., W. L., Tselioudis, G., Wang, H., Zeng, X., and Zuidema, P.: An
 1159 Overview of Atmospheric Features Over the Western North Atlantic Ocean and North American
 1160 East Coast – Part 2: Circulation, Boundary Layer, and Clouds, J Geophys Res-Atmos,
 1161 10.1029/2020JD033423, 2021.
 1162 Papritz, L., Pfahl, S., Sodemann, H., and Wernli, H.: A Climatology of Cold Air Outbreaks and
 1163 Their Impact on Air-Sea Heat Fluxes in the High-Latitude South Pacific, J Climate, 28, 342-364,
 1164 10.1175/Jcli-D-14-00482.1, 2015.
 1165 Pedregosa, F., Varoquaux, G., Gramfort, A., Michel, V., Thirion, B., Grisel, O., Blondel, M.,
 1166 Prettenhofer, P., Weiss, R., Dubourg, V., Vanderplas, J., Passos, A., Cournapeau, D., Brucher,
 1167 M., Perrot, M., and Duchesnay, E.: Scikit-learn: Machine Learning in Python, J Mach Learn Res,
 1168 12, 2825-2830, 2011.

Formatted: EndNote Bibliography

1169 Penner, J. E., Xu, L., and Wang, M. H.: Satellite methods underestimate indirect climate forcing
 1170 by aerosols, *P Natl Acad Sci USA*, 108, 13404-13408, 10.1073/pnas.1018526108, 2011.
 1171 Persson, C., Bacher, P., Shiga, T., and Madsen, H.: Multi-site solar power forecasting using
 1172 gradient boosted regression trees, *Sol Energy*, 150, 423-436, 10.1016/j.solener.2017.04.066,
 1173 2017.
 1174 Quaas, J., Boucher, O., and Lohmann, U.: Constraining the total aerosol indirect effect in the
 1175 LMDZ and ECHAM4 GCMs using MODIS satellite data, *Atmos Chem Phys*, 6, 947-955,
 1176 10.5194/acp-6-947-2006, 2006.
 1177 Quaas, J., Boucher, O., Bellouin, N., and Kinne, S.: Satellite-based estimate of the direct and
 1178 indirect aerosol climate forcing, *J Geophys Res-Atmos*, 113, 10.1029/2007jd008962, 2008.
 1179 Quinn, P. K., Coffman, D. J., Johnson, J. E., Upchurch, L. M., and Bates, T. S.: Small fraction of
 1180 marine cloud condensation nuclei made up of sea spray aerosol, *Nature Geoscience*, 10, 674-679,
 1181 10.1038/ngeo3003, 2017.
 1182 Randles, C. A., da Silva, A. M., Buchard, V., Colarco, P. R., Darmenov, A., Govindaraju, R.,
 1183 Smirnov, A., Holben, B., Ferrare, R., Hair, J., Shinozuka, Y., and Flynn, C. J.: The MERRA-2
 1184 Aerosol Reanalysis, 1980 Onward. Part I: System Description and Data Assimilation Evaluation,
 1185 *J Climate*, 30, 6823-6850, 10.1175/Jcli-D-16-0609.1, 2017.
 1186 [Reutter, P., Su, H., Trentmann, J., Simmel, M., Rose, D., Gunthe, S.S., Wernli, H., Andreae,](#)
 1187 [M.O., Pöschl, U.: Aerosol- and updraft-limited regimes of cloud droplet formation: influence of](#)
 1188 [particle number, size and hygroscopicity on the activation of cloud condensation nuclei \(CCN\).](#)
 1189 [Atmospheric Chemistry and Physics 9, 7067–7080, doi:10.5194/acp-9-7067-2009, 2009.](#)
 1190
 1191 Rolph, G., Stein, A. and Stunder, B.: Real-time Environmental Applications and Display
 1192 sYstem: READY, *Environ. Model. Softw.*, 95, 210–228,
 1193 <https://doi.org/10.1016/j.envsoft.2017.06.025>, 2017.
 1194
 1195 Sekiguchi, M., Nakajima, T., Suzuki, K., Kawamoto, K., Higurashi, A., Rosenfeld, D., Sano, I.,
 1196 and Mukai, S.: A study of the direct and indirect effects of aerosols using global satellite data
 1197 sets of aerosol and cloud parameters, *J Geophys Res-Atmos*, 108, 10.1029/2002jd003359, 2003.
 1198 Shingler, T., Dey, S., Sorooshian, A., Brechtel, F. J., Wang, Z., Metcalf, A., Coggon, M.,
 1199 Mulmenstadt, J., Russell, L. M., Jonsson, H. H., and Seinfeld, J. H.: Characterisation and
 1200 airborne deployment of a new counterflow virtual impactor inlet, *Atmos Meas Tech*, 5, 1259-
 1201 1269, 10.5194/amt-5-1259-2012, 2012.
 1202 Sinclair, K., van Dierenhoven, B., Cairns, B., Alexandrov, M., Moore, R., Ziemba, L. D., and
 1203 Crosbie, E.: Observations of Aerosol-Cloud Interactions During the North Atlantic Aerosol and
 1204 Marine Ecosystem Study, *Geophysical Research Letters*, 47, e2019GL085851,
 1205 <https://doi.org/10.1029/2019GL085851>, 2020.
 1206 Sorooshian, A., Anderson, B., Bauer, S. E., Braun, R. A., Cairns, B., Crosbie, E., Dadashazar,
 1207 H., Diskin, G., Ferrare, R., Flagan, R. C., Hair, J., Hostetler, C., Jonsson, H. H., Kleb, M. M.,
 1208 Liu, H. Y., MacDonald, A. B., McComiskey, A., Moore, R., Painemal, D., Russell, L. M.,
 1209 Seinfeld, J. H., Shook, M., Smith, W. L., Thornhill, K., Tselioudis, G., Wang, H. L., Zeng, X. B.,
 1210 Zhang, B., Ziemba, L., and Zuidema, P.: Aerosol-Cloud-Meteorology Interaction Airborne Field
 1211 Investigations: Using Lessons Learned from the US West Coast in the Design of ACTIVATE off
 1212 the US East Coast, *B Am Meteorol Soc*, 100, 1511-1528, 10.1175/Bams-D-18-0100.1, 2019.
 1213 Sorooshian, A., Corral, A. F., Braun, R. A., Cairns, B., Crosbie, E., Ferrare, R., Hair, J., Kleb, M.
 1214 M., Mardi, A. H., Maring, H., McComiskey, A., Moore, R., Painemal, D., Scarino, A. J.,

Formatted: EndNote Bibliography

Schlosser, J., Shingler, T., Shook, M., Wang, H. L., Zeng, X. B., Ziemba, L., and Zuidema, P.: Atmospheric Research Over the Western North Atlantic Ocean Region and North American East Coast: A Review of Past Work and Challenges Ahead, *J Geophys Res-Atmos*, 125, 10.1029/2019JD031626, 2020.

Stein, A. F., Draxler, R. R., Rolph, G. D., Stunder, B. J. B., Cohen, M. D. and Ngan, F.: NOAA's HYSPLIT Atmospheric Transport and Dispersion Modeling System, *Bull. Am. Meteorol. Soc.*, 96(12), 2059–2077, <https://doi.org/10.1175/BAMS-D-14-00110.1>, 2015.

[Stier, P.: Limitations of passive remote sensing to constrain global cloud condensation nuclei, *Atmospheric Chemistry and Physics* 16, 6595–6607, doi:10.5194/acp-16-6595-2016, 2016.](#)

Storelmo, T., Lohmann, U., and Bennartz, R.: What governs the spread in shortwave forcings in the transient IPCC AR4 models?, *Geophys Res Lett*, 36, 10.1029/2008gl036069, 2009.

Tackett, J. L., Winker, D. M., Getzewich, B. J., Vaughan, M. A., Young, S. A., and Kar, J.: CALIPSO lidar level 3 aerosol profile product: version 3 algorithm design, *Atmos Meas Tech*, 11, 4129–4152, 10.5194/amt-11-4129-2018, 2018.

Terai, C. R., Wood, R., and Kubar, T. L.: Satellite estimates of precipitation susceptibility in low-level marine stratiform clouds, *J Geophys Res-Atmos*, 120, 8878–8889, 10.1002/2015jd023319, 2015.

Thornhill, K. L., Anderson, B. E., Barrick, J. D. W., Bagwell, D. R., Friesen, R., and Lenschow, D. H.: Air motion intercomparison flights during Transport and Chemical Evolution in the Pacific (TRACE-P)/ACE-ASIA, *Journal of Geophysical Research: Atmospheres*, 108, <https://doi.org/10.1029/2002JD003108>, 2003.

Twomey, S.: Influence of Pollution on Shortwave Albedo of Clouds, *J Atmos Sci*, 34, 1149–1152, 10.1175/1520-0469(1977)034<1149:Tiopot>2.0.Co;2, 1977.

Winker, D. M., Vaughan, M. A., Omar, A., Hu, Y. X., Powell, K. A., Liu, Z. Y., Hunt, W. H., and Young, S. A.: Overview of the CALIPSO Mission and CALIOP Data Processing Algorithms, *J Atmos Ocean Tech*, 26, 2310–2323, 10.1175/2009jtecha1281.1, 2009.

Wood, R.: Stratocumulus Clouds, *Monthly Weather Review*, 140, 2373–2423, 10.1175/Mwr-D-11-00121.1, 2012.

[Zhang, Z., Ackerman, A.S., Feingold, G., Platnick, S., Pincus, R., Xue, H.: Effects of cloud horizontal inhomogeneity and drizzle on remote sensing of cloud droplet effective radius: Case studies based on large-eddy simulations, *Journal of Geophysical Research: Atmospheres* 117, doi:10.1029/2012jd017655, 2012.](#)

[Zhang, Z., Werner, F., Cho, H.-M., Wind, G., Platnick, S., Ackerman, A.S., Di Girolamo, L., Marshak, A., Meyer, K.: A framework based on 2-D Taylor expansion for quantifying the impacts of subpixel reflectance variance and covariance on cloud optical thickness and effective radius retrievals based on the bispectral method, *Journal of Geophysical Research: Atmospheres* 121, 7007–7025, doi:10.1002/2016jd024837, 2016.](#)

Formatted: EndNote Bibliography

Formatted: EndNote Bibliography, Space After: 0 pt, Line spacing: single

Formatted: Font: Times New Roman, 12 pt, Font color: Auto, Complex Script Font: 12 pt, Pattern: Clear

Formatted: Font: Times New Roman, 12 pt, Font color: Auto, Complex Script Font: 12 pt, Pattern: Clear

Formatted: Font: Times New Roman, 12 pt, Font color: Auto, Complex Script Font: 12 pt, Pattern: Clear

Formatted: Font: Times New Roman, 12 pt, Font color: Auto, Complex Script Font: 12 pt, Pattern: Clear

Formatted: Font: (Default) Times New Roman, Not Bold, Font color: Auto, Complex Script Font: Times New Roman, Not Bold

Page 39: [1] Formatted Dadashazar, Hossein - (hosseind) 5/16/2021 7:13:00 PM

Font: Not Bold, Complex Script Font: Not Bold

Page 39: [2] Formatted Dadashazar, Hossein - (hosseind) 5/16/2021 7:13:00 PM

Font: Not Bold, Complex Script Font: Not Bold

Page 39: [3] Formatted Dadashazar, Hossein - (hosseind) 5/16/2021 7:13:00 PM

Font: Not Bold, Complex Script Font: Not Bold

Page 39: [4] Formatted Dadashazar, Hossein - (hosseind) 5/16/2021 7:17:00 PM

Font: Not Bold, Complex Script Font: Not Bold